frontiers in Earth Science

ORIGINAL RESEARCH
published: 22 March 2022
doi: 10.3389/feart.2022.853021

Using Eruption Source Parameters and High-Resolution Grain-Size Distributions of the 7.7 ka Cleetwood Eruption of Mount Mazama (Oregon, United States) to Reveal Primary and Secondary Eruptive Processes

Joshua Wiejaczka and Thomas Giachetti*

Department of Earth Sciences, University of Oregon, Eugene, OR, United States

Numerical simulations of real-time volcanic ash dispersal forecasts and ensuing tephra hazard assessments rely on field-derived Eruption Source Parameters (ESPs) such as plume height, erupted volume, mass eruption rate and the Total Grain-Size Distribution (TGSD) of particles ejected from a volcano into the atmosphere. Here we calculate ESPs for the ~7.7 ka Cleetwood eruption of Mount Mazama (Crater Lake/giiwas, Oregon, United States) that immediately preceded the caldera-forming eruption. We also introduce a novel approach to produce high-resolution grain-size distributions (GSDs) of individual samples over a wide range of particle sizes (0.00035–35 mm) by combining laser diffraction with dynamic image analysis. Detailed field analysis allows us to divide the Cleetwood eruptive sequence into a series of two distinct and consecutive VEI 4 eruptions: the lower (~0.98 km^3) and upper (~0.20 km^3) Cleetwood units. The lower Cleetwood was the most intense with a plume height of ~19 km and an average mass discharge rate of ~3.1×10^7 kg s^{-1}. Its TGSD yields a fractal dimension D~3.1, like other similar eruptions. All twelve high-resolution GSDs produced in this study exhibit two systematic breaks in slope from a power-law relationship at ~0.125 and ~0.510 mm. These breaks in slope create three segments: S1 (<0.125 mm), S2 (0.125–0.510 mm), and S3 (>0.510 mm) that can be fit by power-law relationships with fractal dimensions of D1 = 2.5 ± 0.2, D2 = 0.5 ± 0.1, and D3 = 3.6 ± 1.1, respectively. Together with ESPs and detailed componentry, D values at various locations give insight into magma fragmentation and tephra transport. We find that D1 values are positively correlated with the median grain-size and are similar to values found in rapid decompression magma fragmentation experiments. We infer that D1 values reflect the size distribution of the primary products of magma fragmentation and could thus be used to infer the potential energy at fragmentation. We interpret the relatively low values of D2 to an increase in dense components due to particle rafting. Our work shows that comparing high-resolution GSDs at several locations on the dispersal axis can further constrain primary and secondary eruptive processes, which prove crucial to improving tephra hazard assessments and dispersal forecasting.

OPEN ACCESS

Edited by:
Antonio Costa, National Institute of Geophysics and Volcanology, Italy

Reviewed by:
Sebastien Biass, University of Geneva, Switzerland
Fabio Dioguardi, British Geological Survey—The Lyell Centre, United Kingdom

***Correspondence:**
Joshua Wiejaczka
jwiejacz@uoregon.edu

Specialty section:
This article was submitted to Volcanology, a section of the journal Frontiers in Earth Science

Received: *12 January 2022*
Accepted: *07 March 2022*
Published: *22 March 2022*

Citation:
Wiejaczka J and Giachetti T (2022) Using Eruption Source Parameters and High-Resolution Grain-Size Distributions of the 7.7 ka Cleetwood Eruption of Mount Mazama (Oregon, United States) to Reveal Primary and Secondary Eruptive Processes. Front. Earth Sci. 10:853021. doi: 10.3389/feart.2022.853021

Keywords: magma fragmentation, tephra dispersal, grain-size distribution, eruption source parameters, fractal dimension, explosive volcanism

INTRODUCTION

Volcanic plumes and tephra fallout from explosive eruptions are the most far reaching of the volcanic hazards and have the potential to cause fatalities, disrupt the global economy, and affect climate (McCormick et al., 1995; Robock 2000; Sigl et al., 2015; Choumert-Nkolo et al., 2021). Tephra dispersion and sedimentation models are used before and during an eruption to forecast and mitigate impacts to air traffic and communities in the path of an evolving volcanic ash cloud (Bonadonna et al., 2005; Schwaiger et al., 2012). The accuracy of these forecasts largely depends on that of input eruption source parameters (ESPs) such as plume height (H_t), erupted volume (V), mass eruption rate (MER), and the Total Grain-Size Distribution (TGSD) of particles ejected by a volcano into the atmosphere. These initial eruption source parameters are challenging to constrain in real time and thus rely on information obtained from detailed field studies of analogous eruptions. The construction of isopach and isopleth maps and the collection of individual grain size distributions, which are all needed to calculate ESPs, are at times challenging, in part because proximal deposits are usually too thick to be accurately measured and described, and distal deposits are often missing. It is thus crucial to better understand the relationships between eruption source parameters and the characteristics of the deposit (e.g., thickness and grain size distribution as a function of location compared to the vent and main dispersal axis).

The TGSD of a given eruption evolves with time from fragmentation in the conduit to final deposition on the Earth's surface. The primary products of magma fragmentation exhibit cumulative grain-size distributions (i.e., the "primary TGSD") that can be fit with a power-law relationship $(N > d) = \lambda d^{-D}$, where N is the number density of particles, d is the equivalent particle diameter, λ is a scaling factor, and D is the power-law exponent or fractal dimension (Kaminski and Jaupart, 1998; Kueppers et al., 2006; Giachetti et al., 2021). Experimental fragmentation of volcanic products yields D values that are always <3 and mostly around 2.5 ± 0.3 (Turcotte, 1997; Kaminski and Jaupart, 1998; Kueppers et al., 2006; Perugini and Kueppers 2012). Kueppers et al. (2006) further showed that the fractal dimension of the size distributions of the products of experimental magma fragmentation by rapid decompression is positively correlated with the potential energy for fragmentation, and thus that D reflects the explosivity of an eruption. After fragmentation in the conduit, the primary TGSD evolves due to processes that can either increase (e.g., expansion, amalgamation and sintering; Rust and Cashman, 2011; Giachetti et al., 2021) or decrease (e.g., disruption, attrition, comminution, abrasion; Dufek and Manga, 2008; Dufek et al., 2012; Kueppers et al., 2012; Jones and Russell, 2017) the size of pyroclasts, making the TGSD one of the most difficult ESPs to constrain (Pioli et al., 2019). This overprinting of post fragmentation processes on the "final" TGSD of tephra makes the primary TGSD, and thus the potential energy for fragmentation, challenging to determine. Additionally, the TGSD that needs to be implemented in tephra dispersion and deposition models (e.g., Tephra2, Bonadonna et al., 2005; FALL3D, Folch et al., 2020; NAME, Jones et al., 2007; Ash3D, Schwaiger et al., 2012), and its evolution with time and space, are poorly constrained because both the location and extent of secondary fragmentation in the conduit and/or the plume remain unclear. Provided the processes that affect the final TGSD can be disentangled, the latter can be used to gain information such as the depth and mechanisms of fragmentation, eruption column heights, the state of the magma at fragmentation, and the energy released by explosive fragmentation (Kueppers et al., 2006; Perugini and Kueppers, 2012; Rossi et al., 2019).

The final TGSD of an explosive eruption, later simply referred to as "TGSD," is interpolated from individual grain-size distributions (GSDs) of the tephra deposit measured after the eruption at multiple locations (e.g., Murrow et al., 1980; Walker 1980; Walker 1981a; Walker 1981b; Sparks et al., 1981; Carey and Sigurdsson 1982; Parfitt 1998; Bonadonna and Houghton 2005; Costa et al., 2016; Pioli et al., 2019). Due to secondary fragmentation and transport-related processes, individual GSDs vary from location to location and differ from both the final TGSD (Pioli et al., 2019; Mele et al., 2020) and the primary TGSD (Kaminski and Jaupart, 1998; Dufek et al., 2012; Giachetti et al., 2021). How these GSDs vary with direction, distance from the vent, and ESPs can illuminate processes that occur during transport and affect particles differently depending on their size, density, and shape (e.g., ash aggregation; Rose and Durant, 2011; Saxby et al., 2018; Rossi et al., 2021). It might thus be possible to glean information about both primary and secondary eruptive processes by comparing detailed GSDs of a single deposit obtained at different locations.

In this study, we calculate ESPs for the ~7.7 ka Cleetwood eruption of Mount Mazama (Crater Lake/giiwas, Oregon, United States; Young 1990), which immediately preceded the climactic caldera-forming eruption of the same volcano, one of the largest eruptions of the Holocene (Bacon, 1983; Buckland et al., 2021). Additionally, we apply a novel approach to produce high-resolution grain-size distributions of tephra samples over the range 0.00035–35 mm, by combining laser diffraction and dynamic image analysis techniques. Together with ESPs and detailed componentry, the high-resolution of these grain-size distributions from individual locations within the Cleetwood deposit provides insight into magma fragmentation, tephra transport, and how the Cleetwood eruption evolved over time.

GEOLOGIC BACKGROUND

Mount Mazama

Located in Oregon in western North America, Mount Mazama is one of the major stratovolcanoes making up the Cascade Volcanic

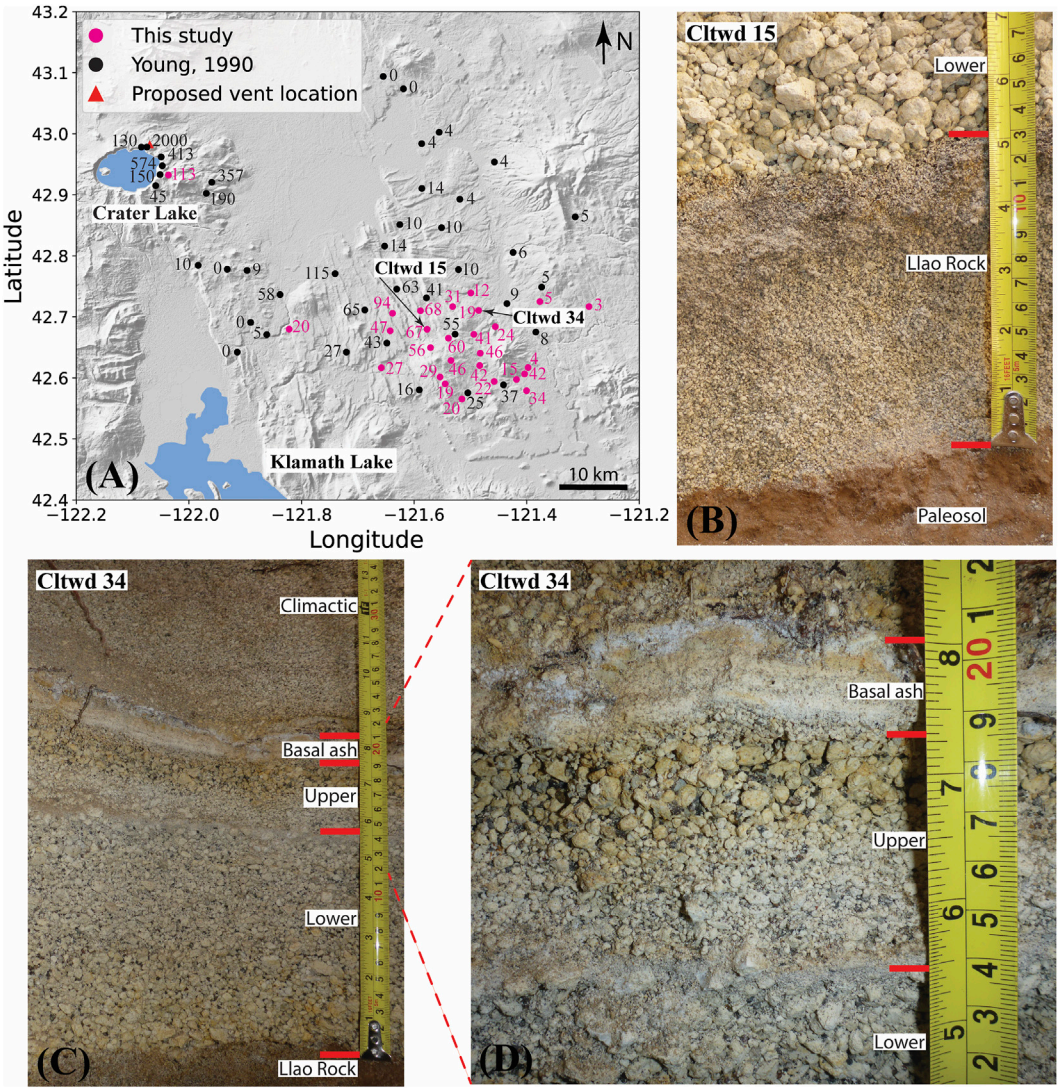

FIGURE 1 | (A) Location of collected samples with total Cleetwood eruption thicknesses (cm) from this study, in pink, and Young (1990), in black. Proposed vent location from Bacon (1983) and background is global Earth relief (Tozer et al., 2019). **(B)** Photograph showing all of Llao Rock and the contact between Llao Rock and lower Cleetwood at location Cltwd 15. Note the drastic increase in size of pyroclasts from Llao Rock to lower Cleetwood. **(C)** Stratigraphic sequence showing lower Cleetwood, upper Cleetwood, and the overlying Climactic deposit at location Cltwd 34. Llao Rock is not present at this location. **(D)** Closeup photograph showing the end of lower Cleetwood, upper Cleetwood, and the Basal ash layer, which marks the beginning of the Climactic deposit (Young, 1990). Note the gray fine ash layer defining the boundary between lower Cleetwood and upper Cleetwood. Measuring tape is in both inches (left) and centimeters (right).

Arc. Mount Mazama is especially known for the approximately 8 × 10 km^2 caldera that formed during the ~7.7 ka climactic eruption and which now contains Crater Lake (referred to as giiwas by the Klamath tribes) within it. The Mazama edifice began forming ~420 ka ago with the emplacement of basaltic andesite to dacitic lava flows. Mainly effusive activity continued until ~27 ka ago with andesitic and dacitic compositions being volumetrically dominant (Bacon, 1983). The eruption of a rhyodacitic lava flow ~27 ka ago marked the first eruption from the magma chamber that would later serve the climactic caldera-forming eruption (Bacon and Lanphere, 2006). The climactic eruption was preceded by two Plinian eruptions, Llao Rock and Cleetwood. The ~7.9 ka Llao Rock eruption deposited a tephra fall unit of 2.27 km^3 (non-DRE) followed by a rhyodacitic lava flow of ~0.5 km^3 (Bacon, 1983; Young, 1990). The Cleetwood eruption (described in detail below) followed and began with a Plinian phase that erupted a total of 1.54 km^3 (non-DRE) of pyroclastic fall material according to Young (1990). Explosive activity then transitioned to an effusive stage, with no apparent break, extruding a rhyodacitic lava flow with a minimum volume of ~0.6 km^3 (Bacon, 1983). Although the exact timing of the Cleetwood eruption is still unclear, the back-flowing of the Cleetwood flow into the caldera and the fact that pumice from the climactic eruption are oxidized and welded to the top of the

Cleetwood flow suggest that it occurred within weeks to no more than 100 years before the onset of the climactic eruption (Bacon, 1983; Kamata et al., 1993). The climactic caldera-forming eruption of Mount Mazama occurred 7,633 ± 49 cal yr BP (Egan et al., 2015) in two distinct but continuous phases and erupted ~176 km^3 of tephra (61 km^3 DRE; Buckland et al., 2020). The first phase consisted of a single-vent Plinian eruption followed by column collapse and the emplacement of the Wineglass Welded Tuff ignimbrite. The second, ring-vent phase produced a voluminous ash-flow and led to the formation of the caldera (Bacon, 1983; Young, 1990). The products forming four volcanic edifices were erupted after the caldera formed, with the extrusion of a 0.074 km^3 unnamed dome ~4.8 ka ago being the most recent volcanic activity at Crater Lake (Bacon et al., 2002).

The Cleetwood Eruption

To the best of our knowledge, all currently available information concerning the physical characteristics of the Cleetwood eruption of Mount Mazama comes from the works of Bacon (1983), Young (1990), Bourgeois (1998), and Wearn (2002). A summary of these studies related to the main deposit features and eruptive parameters is provided here.

The vent associated with the Cleetwood deposit is allegedly located near Cleetwood Cove in the low hills NE of the Crater Lake Rim Drive (Bacon, 1983) (**Figure 1**). At ~35 km ESE of this vent, the Cleetwood tephra deposit is still >1 m thick and exhibits two units, the main Cleetwood and the thinner upper Cleetwood, following Young's nomenclature (Young, 1990). The main Cleetwood unit (1.15 km^3 non-DRE; Young, 1990) is characterized by strong normal grading and presents two distinct normally graded packages in thicker sections. The break within the main Cleetwood unit does not affect the overall normal grading of the unit and does not represent a significant pause in eruptive activity (Young, 1990). The upper Cleetwood unit (0.39 km^3 non-DRE; Young, 1990) is characterized by strong reverse grading, with a grey ash layer at the base that rapidly grades into coarser material primarily composed of pumice and obsidian pyroclasts. Due to the nature of proximal deposits and their tendency to obscure characteristics created from changes in eruption dynamics, the main and upper Cleetwood units are indistinguishable at exposures on the caldera walls (Cleetwood Cove, Wineglass, and Skell Head; Young, 1990; Bourgeois, 1998). The Cleetwood fall deposit is ~20 m thick at Cleetwood Cove, where individual lithic blocks can reach up to 1 m in diameter. This location contains alternating layers of lapilli/blocks and ash that decrease in thickness upwards through the section. The ash layers have been interpreted as intra-Plinian pyroclastic flows (Young, 1990).

The Cleetwood deposit is poor in finer material. In medial deposits where two distinct packages are present, lithic content is highest at the base of both packages and generally decreases with stratigraphic height. The abundance of lithics at these two positions within the stratigraphy suggests vent initiation and clearance (Young, 1990). Obsidian pyroclasts are the most abundant in the upper Cleetwood unit and generally increase with stratigraphic height at proximal exposures. The general decrease in lithics and increase in obsidian pyroclasts with time suggests a conduit that is progressively annealed with obsidian. This annealed obsidian is later eroded during the final explosive phase (Young, 1990; Bourgeois, 1998; Wearn, 2002). Observations at proximal locations suggest that the eruption column was sustained through time (Bourgeois, 1998), although the normally graded main Cleetwood unit and the reversely graded upper Cleetwood unit indicate fluctuations in column height. The Cleetwood eruption is estimated to have an initial column height of 30 ± 5 km and an average mass eruption rate of $(2 \pm 1)\times10^8$ kg s^{-1} (Young, 1990). Explosive activity then transitioned to an effusive stage, with no apparent break, and extruded a ~0.6 km^3 rhyodacitic lava flow. ESPs and the continuity of the Cleetwood eruption are reevaluated herein.

METHODS AND MATERIALS

Field

Field work was conducted in 2018 and 2021 on the Cleetwood tephra fall deposit, 6–71 km southeast of the proposed vent location (**Figure 1**). Twenty-eight pits were dug by hand until the bottom of the Cleetwood tephra deposit was reached. At each location, the deposit was divided into subunits based on visible changes in grading, particle size, color, and/or componentry, if applicable. Subunits were then described in detail, measured for their thickness, photographed, and several hundred grams to a few kilograms of each subunit were collected. Sampling the Cleetwood deposit itself was sometimes challenging due to the massive amount of tephra produced by the climactic eruption of Mount Mazama that lie atop the Cleetwood tephra fall, reaching up to 2.3 m in this field area depending on sampling location.

Laboratory Analyses

All samples collected at the 28 locations visited were analyzed for mass distribution by sieving and weighing. Samples from three locations, Cltwd 5, Cltwd 17, and Cltwd 18, respectively located at 46 km, 56 km, and 66 km from the proposed vent and roughly on the main dispersal axis of the Cleetwood eruption, were further analyzed for high-resolution grain-size distributions. Componentry was realized on all samples collected at Cltwd 5. We encourage the reader to use **Figure 2** to follow our analytical protocol described thereafter.

High-Resolution Grain-Size Distribution

Individual Analyses

Tephra samples from each subunit were first dried in a convection oven at 100°C for 24 h to remove adsorbed water (**Figure 2A**). Bulk samples (kilograms) were split into workable aliquots (10's of grams) using a Humboldt testing equipment sample splitter (**Figure 2B**). Each aliquot was then manually sieved into twelve discrete sieve size fractions: 0–0.032 mm, 0.032–0.063 mm, 0.063–0.125 mm, 0.125–0.25 mm, 0.25–0.5 mm, 0.5–1 mm, 1–2 mm, 2–4 mm, 4–8 mm, 8–16 mm, 16–32 mm and 32–64 mm (i.e., every phi size from

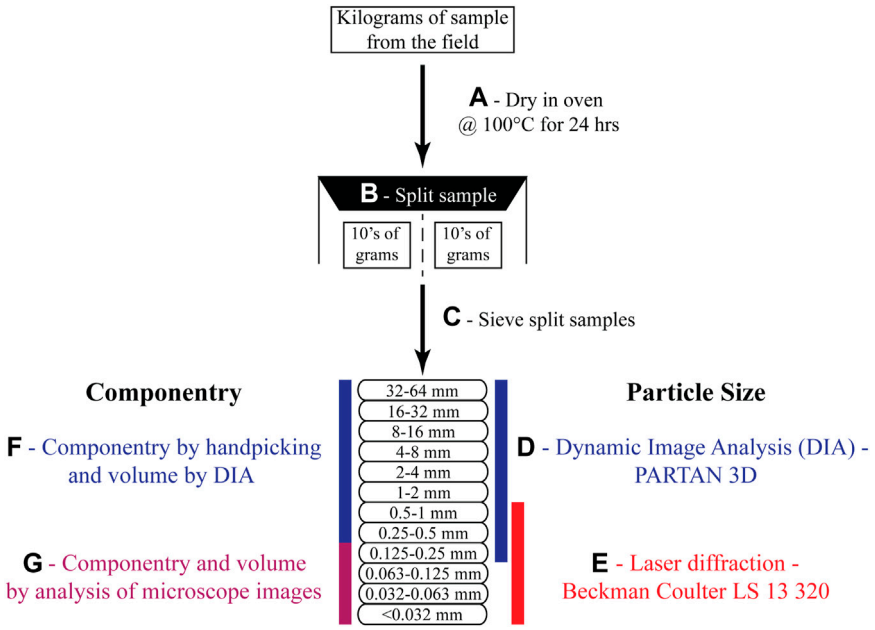

FIGURE 2 | Summary of the workflow steps of our study. **(A)** All samples collected from the field were dried in an oven at 100°C for 24 h to remove adsorbed water. **(B)** Samples were then split into workable aliquots of tens of grams each. **(C)** Split samples were manually sieved into twelve discrete size fractions. **(D)** Dynamic image analysis was performed on size fractions 0.125–0.25 mm and larger. **(E)** Laser diffraction analysis was performed on size fractions 0.5–1 mm and smaller. **(F)** Componentry for particles in size fractions 0.25–0.5 mm and larger was determined via handpicking under a stereo microscope and analyzing particle volumes using DIA. **(G)** Componentry and volume of particles in size fractions 0.125–0.25 mm and smaller were determined via microscope images.

−5 to 5; **Figure 1C**). Each size fraction was then weighed using a high-precision balance before high-resolution particle size analysis. Sieving was carried out before size analysis to 1) prevent larger particles from obscuring smaller ones during the analysis, which improves accuracy and precision of data collected *via* both Dynamic Image Analysis (DIA) and laser diffraction techniques, and 2) to allow for the measurement of the average density of the bulk tephra fall deposit at each size fraction, which is needed to convert masses to volumes and vice versa.

The size of each particle from each size fraction >0.125 mm was measured *via* DIA using a Microtrac PARTAN 3D particle size and shape analyzer at the University of Oregon (**Figure 1D**; Trafton and Giachetti, 2021). In this apparatus, particles travel along a vibrating tray and fall and rotate in front of a LED backlit screen. Once in freefall, a high-speed, high-resolution camera (100 fps, 15 μm px^{-1}) tracks and records images of all individual particles, taking up to twelve images of each particle. Unlike other DIA instruments, the Microtrac PARTAN 3D uses multiple images of individual particles to measure their size and shape. Using multiple images of individual particles to determine these parameters is critical given the multitude and often extreme shapes of volcanic particles (Riley et al., 2003; Liu et al., 2015). The PARTAN 3D theoretically allows for the measurement of particles from 0.035 to 35 mm, but we found the analysis of volcanic ash <0.125 mm cumbersome and poorly reproducible due to static attraction between particles forming aggregates and thus did not analyze particles <0.125 mm with this instrument. For each particle analyzed, the PARTAN 3D provides, amongst other parameters, the particle size (volume, equivalent diameter) and shape parameters (e.g., form factor, axial ratio, solidity, convexity), thus creating a list of hundreds to hundreds of thousands of lines for each size fraction. Altogether, 10^4–10^6 particles >0.125 mm were individually analyzed per sample using this technique. This method is non-destructive and multiple analyses of individual batches of particles show very good reproducibility for particles >0.125 mm. Only size measurements, not shape, were used in this study.

Size measurements on aliquots of particles 0–1 mm were carried out using laser diffraction on a Beckman Coulter LS 13 320 at the USGS Cascades Volcano Observatory (**Figure 2E**; Blott and Pye, 2006). Although this method does not output an exact number of particles analyzed, we estimate that ~10^5–10^7 particles from each subunit were measured using this technique based on the volume of aliquots used and size distributions obtained. This instrument provides information on particle size in the form of volume fraction as a function of an equivalent diameter, in 93 logarithmic bins regularly spaced from 0.00038 to 2 mm. It does not provide information on particle shape, but rather assumes that particles are spherical to calculate their equivalent diameter.

Combining Datasets

Size data for size fractions 0.125–0.25 mm, 0.25–0.5 mm, and 0.5–1 mm were obtained using both DIA and laser diffraction (**Figures 2D,E**, **Figure 3**), allowing for a comparison and

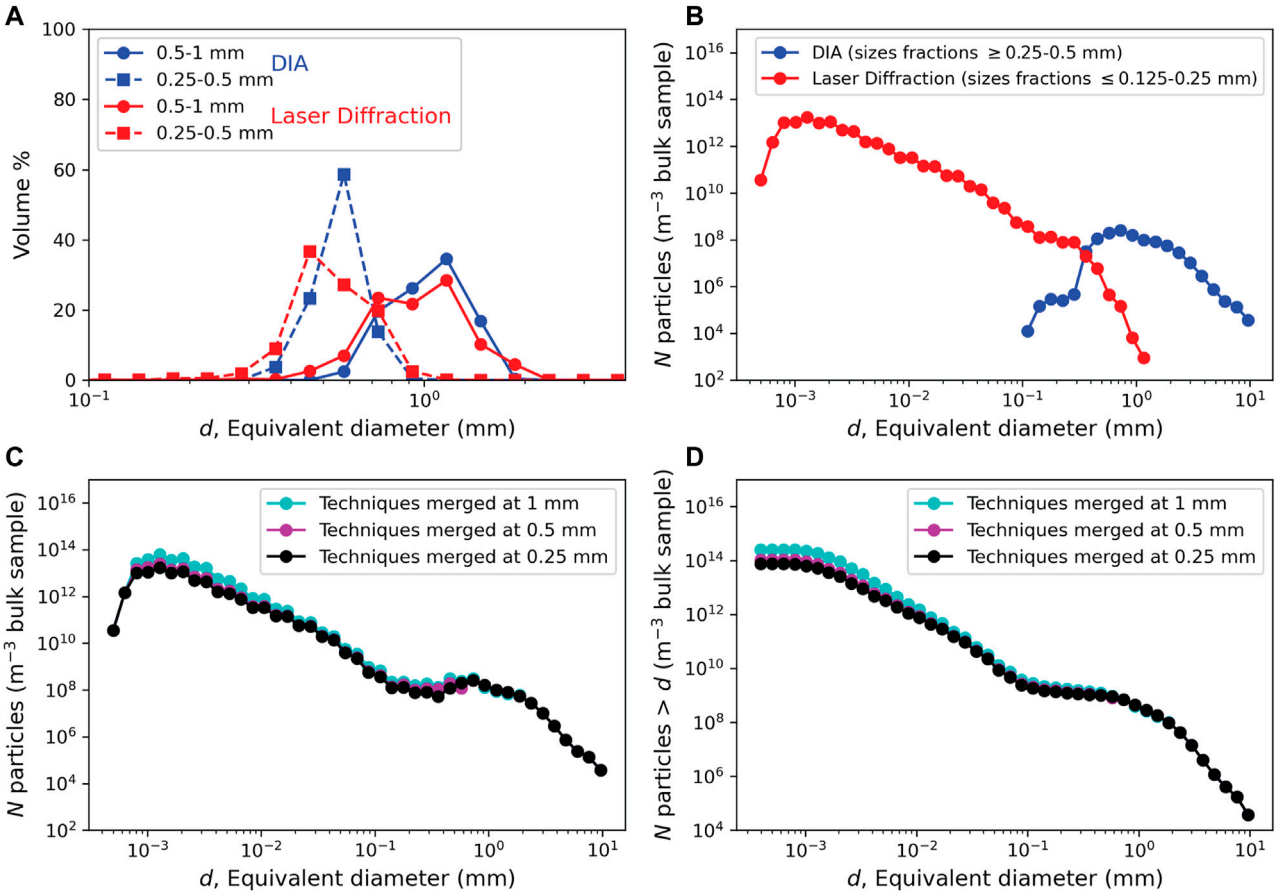

FIGURE 3 | (A) Volume % as a function of equivalent diameter, *d*, for DIA and laser diffraction analyses of two identical size fractions (0.25–0.5 and 0.5–1 mm). Note that for the size fraction 0.25–0.5 mm, the volume % peak for DIA occurs at larger sizes compared to the laser diffraction technique, due to the way the volume of particles is measured (spherical assumption in laser diffraction, whereas shape is measured and thus taken into account using DIA). **(B)** Number density of particles per cubic meter of bulk sample, *N*, as a function of their equivalent diameter, *d*, showing the overlap between laser diffraction and dynamic image analysis (DIA) data. Each curve is an amalgamation of data obtained for several size fractions using a single technique. Sample used here is Cltwd 5A. **(C-D)** Number density, *N*, and cumulative number density ($N > d$) of particles per cubic meter of tephra plotted as a function of equivalent diameter, *d*. These graphs illustrate the impact of choosing different cutoffs (0.25, 0.5, or 1 mm) when merging data from DIA and laser diffraction. Note that the break in slope occurs at the same position regardless of the cutoff and thus is not an artifact of data combination.

combination of the two datasets. Because the PARTAN 3D gives the size of individual particles whereas laser diffraction provides volume fractions, some conversions and re-binning of the data need to be performed before comparing and combining the datasets. In this study, results are sorted and presented in 50 logarithmic bins from 0.00035 to 35 mm, and both the distributions of mass and number density of particles as a function of their size are used.

Data collected by laser diffraction for each size fraction were first converted from volume percent to an actual volume using the mass and density of the size fraction. For each size fraction of each sample, the bulk density of the tephra sample was calculated by dividing the mass of all particles, obtained using a high-precision balance, by the volume they represent. For size fractions 0.125–0.25 mm, 0.25–0.5 mm, and 0.5–1 mm, that volume is the sum of the volumes of all particles analyzed by DIA within that size fraction. For size fractions 0–0.032 mm, 0.032–0.063 mm, and 0.063–0.125 mm, density of the bulk tephra was determined directly using helium pycnometry (Micromeritics AccuPyc II 1340), assuming all particles at these sizes are vesicle-free, which was confirmed by observation under the microscope. Next, the number of particles for each bin was calculated by assuming spherical particles (as assumed when using laser diffraction technique) and dividing the total volume of each bin by the volume of a single particle with a diameter equal to the middle of the bin (**Figure 3B**). For DIA, individual particles are analyzed, and the number of particles per bin was thus obtained directly. Number of particles per cubic meter of tephra was then calculated by dividing the number of particles per bin by the total volume of the sample analyzed. Finally, to produce a single distribution, we use laser diffraction data obtained on all size fractions 0–0.25 mm and DIA data for all size fractions >0.25 mm (**Figure 3C**). Note that we present the data as cumulative number density in most plots (**Figure 3D**). We refer to these individual Grain Size Distributions as GSDs in the paper.

Componentry

Previously split samples (10s of grams) for each discrete size fraction were further split into aliquots of a few grams using a SOILTEST sample splitter to be analyzed for componentry. For size fractions ≥0.25 mm, all particles of the aliquot were handpicked and sorted into one of the following components using a stereomicroscope: pumice, banded pumice, obsidian pyroclast, lithic, and loose crystal (**Supplementary Figure 1**). Once separated, all particles of each component were analyzed using the Microtrac PARTAN 3D to measure the relative volume of all components in each size fraction. For size fractions 0.063–0.125 mm and 0.125–0.25 mm, images of the bulk sample were taken with a Leica M80 stereo microscope and individual particles were outlined based on type. The area of particle outlines from each component category was then calculated using the Fiji (ImageJ) image processing package (Schindelin et al., 2012), and particle volumes were calculated assuming a spherical shape. Upon visual inspection under the stereo microscope, all particles below 0.063 mm were classified as pumice. Altogether, 1,315–2,856 particles from each subunit were sorted.

Eruption Source Parameters

Erupted Volume

Isopach maps were constructed using field data from this study and work done by Young (1990). Isolines were manually drawn on Adobe Illustrator, and the area enclosed by each isoline was then calculated using the Fiji (ImageJ) image processing package. Airfall volume was calculated using *TephraFits* (Biass et al., 2019), which allows the user to best fit thickness (T, in cm) as a function of the square root of area ($\sqrt{A}$, in km) enclosed by each isoline using an exponential (Fierstein and Nathenson 1992; Bonadonna and Houghton 2005), a power-law (Bonadonna and Houghton 2005), or a Weibull (Bonadonna and Costa 2012) equation. To assess the uncertainty in our volume calculations we also ran *TephraFits* in probabilistic mode, which uses the stochastic methodology of (Biass et al., 2014). We applied a 10% uncertainty to both our thickness and area measurements in accordance with the uncertainties associated with isopach construction as quantified in the literature (Le Pennec et al., 2012; Engwell et al., 2013; Klawonn et al., 2014a; Klawonn et al., 2014b). For statistical significance we performed a Monte Carlo simulation of 100,000 runs. Volumes are then reported as a median value with a confidence interval of fifth-95th percentiles.

Plume Height and Mass Eruption Rate

The maximum lithic (ML) size at each location was determined by averaging the diameter of the three largest clasts measured using digital calipers. Maximum lithic isopleth maps were then constructed using data from this study and from Young (1990), when possible. The same method for drawing isopach maps was used to construct the ML isolines (see above). Downwind and crosswind distances were then calculated using Fiji. Plume height, H_t (km), was calculated using the models of Carey and Sparks (1986) and Rossi et al. (2019) hereafter referred to as *CS86* and *R2019*, respectively. The mass eruption rate (*MER*, in kg/s) was then calculated using the model of Mastin (2014), where $MER = 140 \times H_t^{4.15}$ and H_t is the plume height expressed in km.

Total Grain-Size Distribution (TGSD)

The TGSD was determined by applying the Voronoi tessellation method of Bonadonna and Houghton (2005) to the 24 sieved-mass GSDs for all sample locations containing lower Cleetwood (see Results). This method divides a tephra deposit into Voronoi polygons in which all interior points are closer to, and best represented by, a central sample point (centroid). The TGSD is then calculated by multiplying the GSD of the centroid by the area fraction of its Voronoi polygon and summing all weighted GSDs. TGSD is presented herein as a cumulative number density. To determine the number density for a given grain-size, the mass (wt.%) of each phi size (−5 to 5) was first converted to a volume using a density model (**Supplementary Table 1**). Following Bonadonna and Phillips (2003), this model assumes a constant density of 2,380 kg/m^3 (i.e., the density of the glass as determined *via* helium pycnometry of crushed pumices) for particles smaller than 0.063 mm, a constant density of 455 kg/m^3 for particles larger than 2 mm, calculated by dividing the mass of all particles >2 mm by their volume determined *via* DIA, and a linear increase in density between these bounds. Next, the number of particles was calculated by assuming spherical particles and dividing the total volume of each phi size by the volume of a single particle with a diameter equal to the mid interval between phi sizes. Finally, number density (m^{-3}) was calculated by dividing the number of particles per bin by the total volume of all phi sizes (−5 to 5).

RESULTS

Field Observations and Measurements

Twenty-eight pits were dug by hand to the ESE of Crater Lake (**Figures 1**, **4**), covering the proximal and medial parts of the Cleetwood fall deposit. The Cleetwood and overlying Climactic deposits at these locations range from 2.5–113 cm and 12–232 cm in thickness, respectively. Based on abrupt changes in grain size and grading, we further divide the main Cleetwood unit of Young (1990) into two discrete phases (Llao Rock and lower Cleetwood). Young's upper Cleetwood unit is hereafter referred to as upper Cleetwood, and we thus describe and discuss the results concerning these three phases, Llao Rock, lower Cleetwood, and upper Cleetwood, from oldest to youngest.

Llao Rock is identified up to ~63 km SE of the proposed vent location (**Figure 4A**). Its dispersal axis generally trends to the SE with the terminus trending more towards the South. The dispersal area for Llao Rock is narrow and its thickness decreases drastically perpendicular to the main axis. Of the three phases, Llao Rock has the finest particles overall. At Cltwd 5, located 46 km SE of the vent, Llao Rock is 28 cm thick and can be divided into three subunits: A, B, and C, with 5A being the bottommost subunit (**Figure 5**). At Cltwd

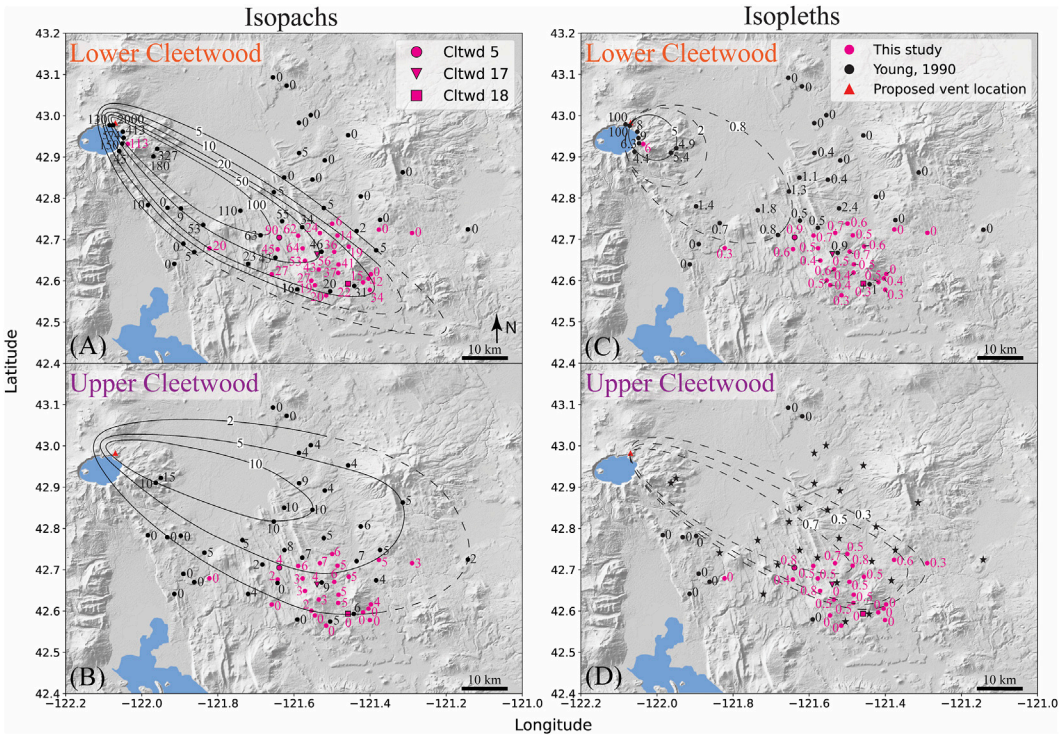

FIGURE 4 | (A-C) Isopach maps for Llao Rock, lower Cleetwood, and upper Cleetwood of the Cleetwood eruption, respectively. **(D-F)** Maximum lithic (ML) isopleth maps for Llao Rock, lower Cleetwood, and upper Cleetwood respectively. Stars on the upper Cleetwood isopleth map represent locations where upper Cleetwood is present, but no ML data is available. All isolines are notated in centimeters. Background is global Earth relief (Tozer et al., 2019).

5, subunit A makes sharp contact with the paleosol and contains ~15% of lithics at size fractions <1 mm. This subunit A normally grades into the middle subunit B. Along with the shift to finer grainsizes, there is also a visible shift in pumice color, from white-grey in A to more brown in B. The uppermost subunit C of Llao Rock is slightly coarser than subunit B and the pumice color shifts back to white-grey. The amount of lithics slowly decreases from bottom to top of Llao Rock. These subunits of P1 are visible at other medial locations.

Lower Cleetwood makes up most of the Cleetwood fall deposit and is 90 cm thick at Cltwd 5 (**Figure 4B**; **Figure 5**). Like Llao Rock, the dispersal axis of lower Cleetwood trends to the SE but the dispersal area is wider. This phase is characterized by a single, normally graded unit at all locations. Pumices, which make up most of the deposit of lower Cleetwood, are white-grey and reach up to 5 cm in diameter at the base of lower Cleetwood in medial locations. Like Llao Rock, the base of lower Cleetwood contains ~15% lithics but with a shift to coarser lithic sizes. The contact between Llao Rock and lower Cleetwood is sharp with no visible signs of erosion, a feature that is found in all pits where both units are present. This led us to divide the "main Cleetwood" unit of Young (1990) into Llao Rock and lower Cleetwood.

Upper Cleetwood is present up to ~80 km ESE of the proposed vent location (**Figure 4C**). Its dispersal axis trends to the ESE and is the widest of the three phases. At medial locations directly East of the vent, Upper Cleetwood is the only phase present. The deposit of upper Cleetwood is characterized by a strong reverse grading (**Figure 4**) and a thin grey ash layer marks the boundary between lower Cleetwood and upper Cleetwood at medial locations SE of the vent. The contact between lower Cleetwood and upper Cleetwood is sharp with no visible signs of erosion. Obsidian pyroclasts are visibly more abundant within upper Cleetwood compared to the other two phases.

Overall, the dispersal axes of Llao Rock, lower Cleetwood, and upper Cleetwood seem to indicate a slight shift in the dominant wind direction from SE to ESE during the Cleetwood eruptive sequence (**Figures 4A–C**).

Individual Grain-Size Distribution

For locations where phases are divided into subunits (e.g., Llao Rock at Cltwd 5: 5A, 5B, and 5C), the thickness fraction of each subunit was used as a weight to calculate the GSD of the whole phase at that location using the individual GSDs of all subunits. Cumulative GSDs of all three phases at Cltwd 5, Cltwd 17, and Cltwd 18 (~46, 56, and 66 km away from the vent) are similar in shape; they show two systematic breaks in slope from a power-law relationship at ~0.125 and ~0.510 mm (**Figure 6A**), creating three individual segments hereafter named S1, S2, and S3 (**Figure 6B**). Each segment can be fit by a power-law relationship, $N > d = \lambda d^{-D}$, where D is the fractal dimension of the segment of the distribution considered. For all three phases, $D1$ values, which

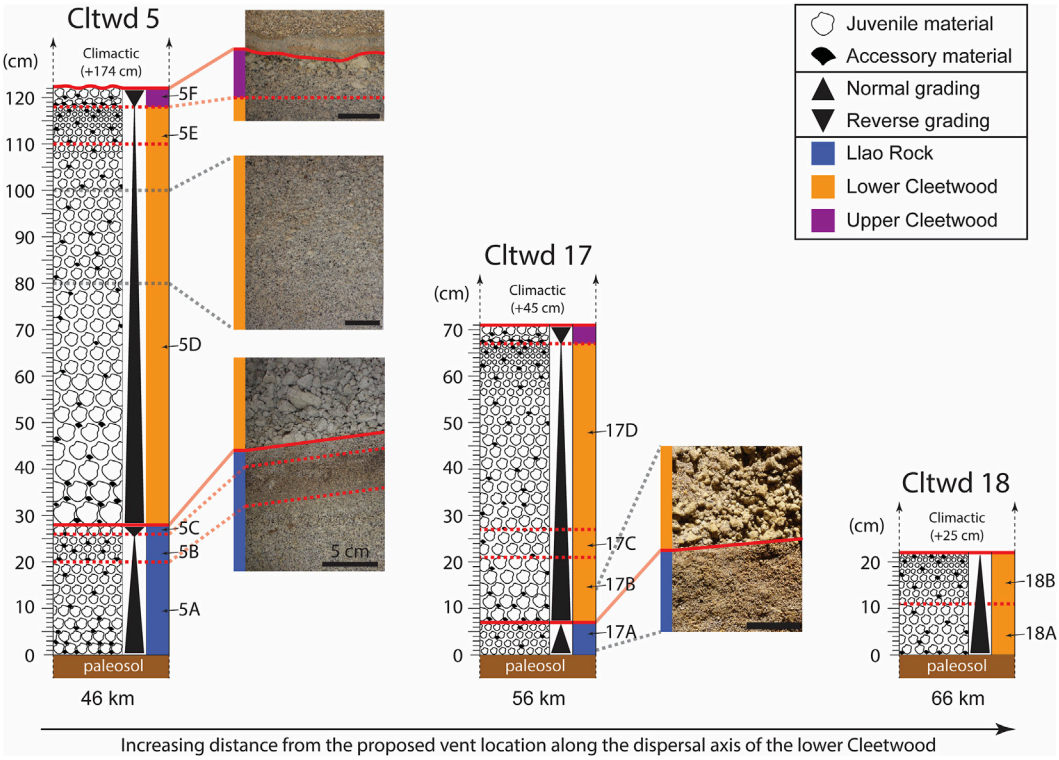

FIGURE 5 | Stratigraphic columns for locations Cltwd 5, 17, and 18, all located on the main dispersion axis of lower Cleetwood and at distances of 46, 56, and 66 km from the proposed vent, respectively (see **Figure 3**). Solid red lines indicate sharp contacts between phases, whereas the dashed red lines divide areas within phases that were subsampled. Scale bar is 5 cm in all photographs. **Cltwd 5** exhibits all three phases of the Cleetwood eruption. Llao Rock makes sharp contact with the paleosol, and three distinct subunits (A, B, C) are observed; subunit A (20 cm) normally grades into subunit B (6 cm) which then reversely grades into the uppermost subunit C (3 cm). Llao Rock and lower Cleetwood make sharp contact and lower Cleetwood (90 cm) is present as a normally graded unit. Upper Cleetwood (4 cm) is reversely graded, a characteristic seen at all locations where it is found. At **Cltwd 17,** all three phases are also observed. Llao Rock (7 cm) makes sharp contact with the paleosol but does not exhibit the three distinct subunits seen at Cltwd 5, it is normally graded. Llao Rock and lower Cleetwood make sharp contact with each other, and lower Cleetwood normally grades until upper Cleetwood. At **Cltwd 18**, only lower Cleetwood (22 cm) is present and found as one normally graded unit that makes sharp contact with the paleosol at its base. At these three locations, the Cleetwood fall deposit is overlayed by 25–174 cm of climactic fall deposit.

correspond to particles <0.125 mm (**Table 1**), range from 2.1–2.7. For a given phase, *D1* does not vary with distance from the vent. Values of *D2*, which correspond to particles ~0.125–0.510 mm in size, are the lowest of all *D*s for all three phases and range from 0.3–0.7. *D2* values slightly increase with distance from the vent for a given phase. Values of *D3*, for particles >0.510 mm, vary the most (2.7–4.7) and increase with distance from the vent for a given phase. Note that the breaks in slope observed on all GSDs are also visible on the DIA and laser diffraction data when considered individually (**Figure 3B**), and thus were not artificially created following the combination of the two datasets.

Componentry

Detailed componentry was realized on samples collected at Cltwd 5, a location ~46 km SE of the proposed vent, on the main dispersal axis of lower Cleetwood and slightly off that of Llao Rock (**Figures 4**, **7**). In all layers of all phases, pumice accounts for at least 92% of the sample's volume. In Llao Rock, pumice is the dominant component at all size fractions, although the proportion of lithics and crystals combined in subunits 5A and 5B reach 30–60 vol.% at sizes 0.063–0.5 mm. The proportion of non-pumice components decreases slightly from 5A to 5B and more significantly from 5B to 5C, with loose crystals being the dominant non-juvenile component in size fractions 0.063–0.5 mm, followed by lithics. Lower Cleetwood is divided into two subunits, 5D (bottom) and 5E (top). Subunit 5D is characterized by an increase in loose crystals compared to the end of Llao Rock (subunit 5C) and by the presence of lithics in size fractions 1–2 mm and 2–4 mm. Subunit 5E marks the end of lower Cleetwood and exhibits an increase in banded pumice (2.9 vol.%) >0.25 mm and a slight increase in both loose crystals (1.7 vol.%) and lithics (2.9 vol.%) at sizes 0.063–1 mm. Upper Cleetwood (subunit 5F) shows an overall increase in both banded pumice and obsidian pyroclasts compared to lower Cleetwood. The proportion of lithics in this phase increases in size fractions 0.5–2 mm, whereas the overall abundance of loose crystals decreases.

Eruption Source Parameters

Bacon (1983) first proposed the vent for the Cleetwood eruption to be located in the low hills northeast of the Rim Road. Applying the source

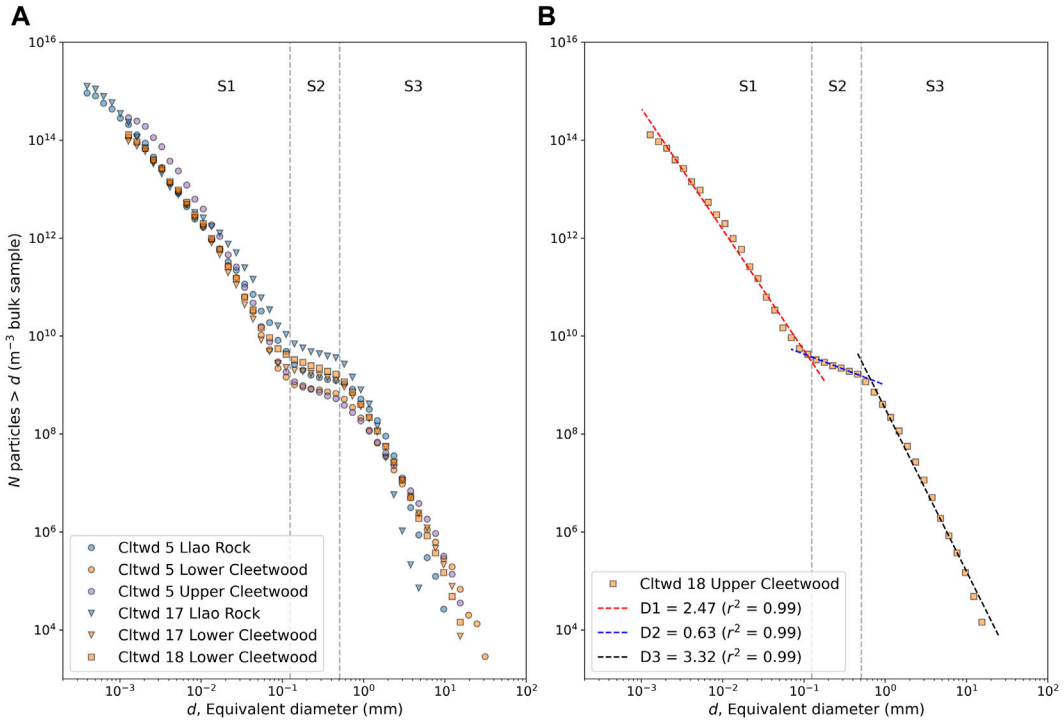

FIGURE 6 | (A) Cumulative number density, *N*, vs equivalent diameter, *d*, for Llao Rock, lower Cleetwood, and upper Cleetwood at Cltwd 5, Llao Rock and lower Cleetwood at Cltwd 17, and lower Cleetwood at Cltwd 18. **(B)** Cumulative number density, *N*, vs equivalent diameter, *d*, for lower Cleetwood at Cltwd 18. Breaks in slope at ~0.125 and ~0.510 mm create three individual segments S1, S2, and S3, which are observed in all distributions (see A). Fractal dimensions (D1, D2, and D3) are obtained by fitting each corresponding segment with a power law, $N > d = \lambda d^{-D}$, where *N* is the number density of particles greater than size *d*, *D* is the fractal dimension, and λ is a scaling factor.

TABLE 1 | Fractal dimension values of cumulative grain-size distributions, D, for deposits present at locations Cltwd 5, 17 and 18 (**Figure 2**; **Figure 4**), together with the r^2 value of the fit. D1, D2, and D3 respectively correspond to the best fits of segments S1 (<0.125 mm), S2 (0.125–0.510 mm), and S3 (>0.510 mm) of the cumulative size distribution (see **Figure 6B**).

Location	Phase	D1	D1 r^2	D2	D2 r^2	D3	D3 r^2
Cltwd 5	Llao	2.25	0.99	0.38	0.98	3.87	0.97
Cltwd 5	Lower	2.62	0.99	0.34	0.99	2.95	0.99
Cltwd 5	Upper	2.70	0.98	0.67	1.00	2.71	0.98
Cltwd 17	Llao	2.08	0.99	0.61	0.97	4.65	0.95
Cltwd 17	Lower	2.58	0.99	0.40	0.99	3.10	0.99
Cltwd 18	Lower	2.47	0.99	0.63	0.99	3.32	0.99

vent locator model of Yang et al. (2019) that uses deposit thickness to find the vent confirms this general location (**Supplementary Figure 2**). The original location of Bacon (1983) lies between the power-law and exponential points generated by the model Yang et al. (2019) and is used as the source vent for all Phases herein.

The erupted volumes (non-DRE) of Llao Rock, lower Cleetwood, and upper Cleetwood of the Cleetwood eruption, calculated both using best fit models (**Figure 8**) and the probabilistic Monte Carlo approach of Biass et al. (2014), are reported in **Table 2**. For each phase, the three methods give volumes that are within 40% of each other using the best fit approach, with the exponential and Weibull methods always giving the best fits (r^2 > 0.99). Calculated volumes are 0.26 ± 0.06 km^3 for Llao Rock, 0.98 ± 0.01 km^3 for lower Cleetwood, and 0.20 ± 0.03 km^3 for upper Cleetwood, making each of these phases a VEI 4 eruption. Volumes obtained using the probabilistic approach are 3–11% larger than using the best fit approach, being 0.29 ± 0.08 km^3 for Llao Rock, 1.01 ± 0.19 km^3 for lower Cleetwood, and 0.21 ± 0.03 km^3 for upper Cleetwood. These results confirm that lower Cleetwood is the most voluminous out of all the phases of the Cleetwood eruption. It is, on its own, close to a VEI 5 eruption.

Llao Rock and upper Cleetwood lack sufficient field constraints to confidently draw isopleth lines for Maximum Lithic (ML) sizes >0.8 cm (**Figures 4D,F**), making it unreliable to use the *CS86* or *R2019* models to calculate a plume height. Consequently, plume height and MER results are presented only for lower Cleetwood in **Supplementary Table 2**. Using *CS86* and averaging the plume heights calculated for the 5, 2, and 0.8 cm ML isolines gives H_t = 25 ± 2 km with an average wind velocity of 27 ± 3 m/s. Comparing this wind velocity with NCEP-DOE Reanalysis 2 data at the entire year of 2020 at Crater Lake (Kanamitsu et al., 2002) shows that this value is reasonable at this location (**Supplementary Figure 3**). Using this H_t and the model of Mastin (2014), the calculated MER for lower Cleetwood is (8.6 ± 3.3)×10^7 kg s^{-1}. Using *R2019*, the

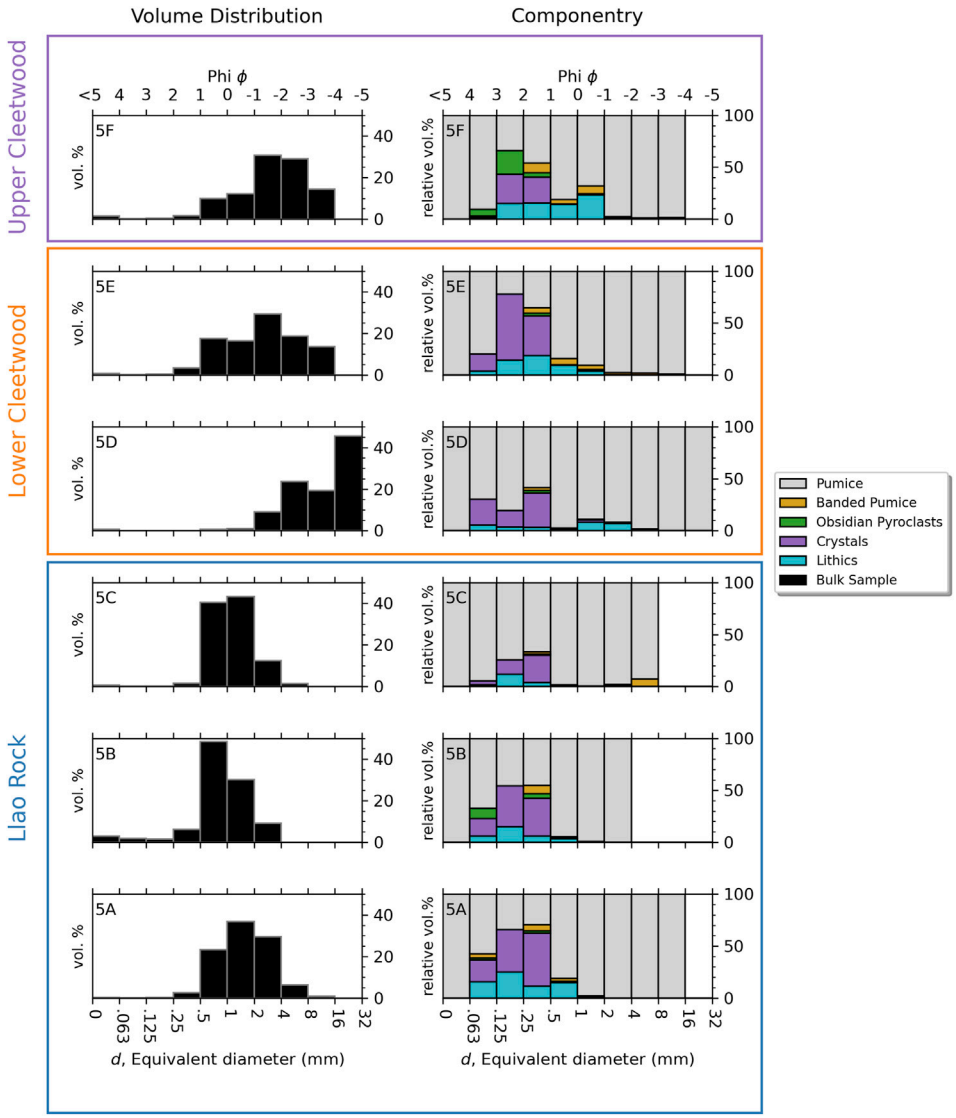

FIGURE 7 | Volume percent of bulk samples (left) and relative volume percent of individual components within each size fraction (right), plotted as a function of equivalent diameter, *d*, for all subunits at location Cltwd 5. Subunits 5A, 5B, and 5C compose Llao Rock, 5D and 5E make up lower Cleetwood, and upper Cleetwood is defined solely by subunit 5F.

more robust model of Rossi et al. (2019), and averaging the plume heights calculated for the 5 and 2 cm ML isolines for eruptive scenarios 2 (intermediate intensity) and 3 (high intensity; see Rossi et al., 2019), gives a plume height of 19 ± 2 km. Given the inadequacies of these models to capture features such as partial column collapse or gravitational fountaining, a large degree of uncertainty is associated with their use. The uncertainty in the above calculated plume height of 2 km falls in line with the ~10% error for strong plumes as determined via the results of a model intercomparison study conducted by Costa et al. (2016). Using this plume height and the model of Mastin (2014), the calculated MER for lower Cleetwood is $(3.1 \pm 1.0)\times10^7$ kg s^{-1}.

As Llao Rock and upper Cleetwood were not present at enough investigated locations within their respective dispersal areas, their TGSDs could not be confidently calculated. The TGSD of lower Cleetwood, calculated using the Voronoi tessellation method of Bonadonna and Houghton (2005) (**Figure 9**), exhibits a power-law relationship, $N > d = \lambda d^{-D}$, where N is the number density of particles, d is the equivalent diameter, λ is a scaling factor, and D is the power-law exponent, or fractal dimension. Best-fitting the TGSD using the least-squares method gives fractal dimension (D) values of 3.0 (r^2 = 0.997), 3.1 (r^2 = 0.997), and 3.2 (r^2 = 0.998) when fitting grain-sizes ≥ 0.5 mm, ≥ 1 mm, and ≥2 mm, respectively. The rationale for only fitting values above 0.5–2 mm is discussed in detail below.

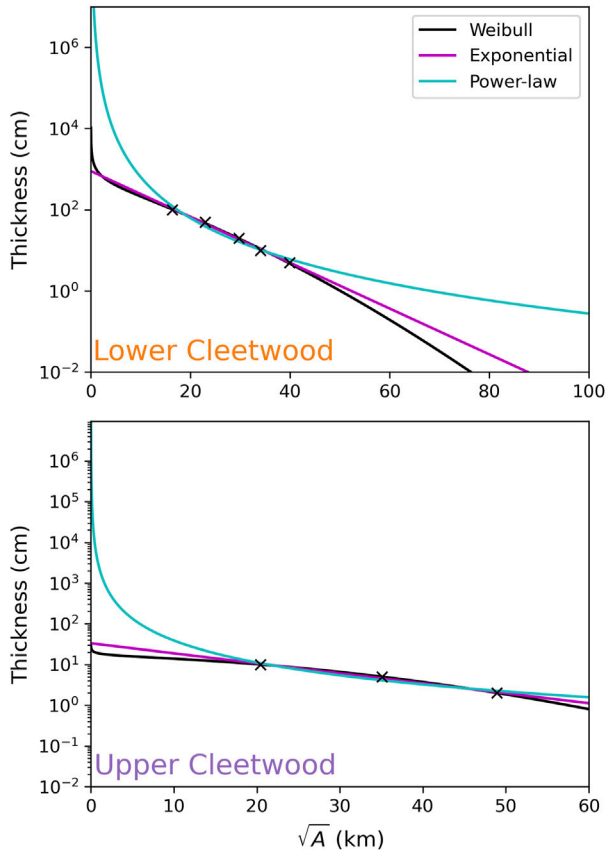

FIGURE 8 | (A-C) Semi-log plots of the thickness of a Phase deposit as a function of the square root of the isopach area and exponential, power-law, and Weibull best fit deposit thinning trends for Llao Rock, lower Cleetwood, and upper Cleetwood, respectively. See **Table 1** for fitting parameters, Pearson correlation coefficients (r^2), and erupted volumes (non-DRE).

DISCUSSION

The Cleetwood Eruptive Sequence

Our results show that the ~7.7 ka Cleetwood eruptive sequence of Mount Mazama consisted of three distinct and consecutive VEI 4 eruptions. Bonadonna and Costa (2012) plotted the relationship between the best fit Weibull parameters θ and λ, along with the total erupted volume derived from their Weibull method for a variety of eruptions ranging from VEI 1 to VEI 6. When plotted together with these data, all three phases of the Cleetwood eruption clearly group with other historic VEI 4 eruptions (**Figure 10**).

Although the plume height, and thus MER, could not be directly calculated for Llao Rock due to a lack of Maximum Lithic (ML) data in the proximal region of the deposit, measurements at locations exhibiting both Llao Rock and lower Cleetwood (**Figures 4D,E**) show that the largest lithics in Llao Rock are consistently much smaller than those in lower Cleetwood. Assuming roughly comparable wind conditions as suggested by the similarities between isopach shapes and dispersal direction of Llao Rock and lower Cleetwood deposits (**Figures 4A,B**), we can confidently infer that the plume height and MER of Llao Rock were lower than 19 km and 3.1×10^7 kg s^{-1}, respectively. As seen in medial locations, Llao Rock can be divided into three subunits that show a slight normal grading during most of Llao Rock, followed by a reverse grading towards the end of this initial phase (**Figure 5**). These fluctuations in grain size may be due to variations in MER throughout Llao Rock, the MER being at its maximum at the onset of the eruption, slowly decreasing throughout most of Llao Rock, before slightly increasing further towards the end of this phase. Lithic content is 4 vol.% at the base of Llao Rock and decreases upward to reach only 0.6 vol.% towards the end of Llao Rock, suggesting that, after vent initiation, minimal vent erosion occurred during this phase.

The sharp contact between Llao Rock and lower Cleetwood at all locations investigated indicates a break between these two phases, and we infer that the deposits of Llao Rock and lower Cleetwood were produced by two distinct plumes, contrary to what was previously suggested (Young, 1990). Although the exact timing between Llao Rock and lower Cleetwood is unknown, we posit that the break in explosive activity was minimal as there are no indications of erosion and/or soil development at their contact.

With an erupted volume of 0.98 ± 0.01 km^3, lower Cleetwood straddles the line between a VEI 4 and VEI 5 eruption and is sub-Plinian following the classification of Bonadonna and Costa (2013, see **Supplementary Figure 4**). Its deposit is characterized by a strong normal grading, which indicates that both plume height (~19 km) and MER (~3.1×10^7 kg s^{-1}) reached a maximum at the beginning of this phase and continuously waned after that. The base of lower Cleetwood appears relatively abundant in lithics in the field compared to the end of Llao Rock (5–10 vol.% of 1–4 mm lithics at the base of lower Cleetwood as opposed to ~0% at the end of Llao Rock, see **Figure 6**), an observation also made by Young (1990) who noted that lithic content was high directly above what he called the "central break in the main Cleetwood," which we interpret as the onset of lower Cleetwood. We agree with Young's interpretation that this relative abundance of lithics at the onset of lower Cleetwood is the result of further conduit/vent clearance. Young's (1990) volume estimate of 1.15 km^3 for his "main Cleetwood" unit includes both what we divided into Llao Rock and lower Cleetwood, which when combined gives 1.24 ± 0.07 km^3. Our results thus slightly revise upwards the volume of these two initial phases of the Cleetwood eruption.

Comparing ML measurements of both lower Cleetwood and upper Cleetwood (**Figures 4E,F**) shows that MLs for upper Cleetwood are only slightly smaller than those of lower Cleetwood at the same location. This suggests that both plume height and MER are only slightly less than lower Cleetwood, although the erupted volume is about five times smaller. The deposit of upper Cleetwood is characterized by a strong reverse grading that suggests an increase in column height and MER with time, likely due to erosional vent widening (Wilson et al., 1980; Carey and Sigurdsson, 1989; Rosi et al., 1999). This vent widening is supported by a slight increase in the proportion of lithics from 3 vol.% to 5 vol.% from lower Cleetwood to upper Cleetwood. Another defining characteristic of upper Cleetwood is the drastic

TABLE 2 | Best fit and probabilistic fitting parameters and erupted volumes obtained using *TephraFits* (Biass et al., 2019) for the three different phases of the Cleetwood eruption.

		Llao Rock	Lower Cleetwood	Upper Cleetwood
Best fit	Exponential Volume (km^3)	0.29 (r^2 = 0.99)	0.99 (r^2 = 0.99)	0.21 (r^2 = 0.99)
	Power-law Volume (km^3)	0.31 (r^2 = 0.96)	0.97 (r^2 = 0.90)	0.22 (r^2 = 0.95)
	Weibull Volume (km^3)	0.19 (r^2 = 0.99)	0.99 (r^2 = 0.99)	0.17 (r^2 = 0.99)
	k_1	-0.1393	-0.1198	-0.0564
	k_2	-	-0.1357	-
	$T0_1$	285.1352	728.67	33.0807
	$T0_2$	-	1.09E+03	-
	M	2.8373	3.3609	1.7886
	CPI	8.22E+04	1.46E+06	2.38E+03
	Θ	80.00	253.06	13.61
	λ	16.10	17.15	35.10
	N	1.70	1.50	1.91
Probabilistic (n = 10^5)	Exponential Volume (km^3)	0.30 ± 0.04	1.04 ± 0.18	0.21 ± 0.02
	Power-law Volume (km^3)	0.31 ± 0.04	1.00 ± 0.15	0.22 ± 0.02
	Weibull Volume (km^3)	0.26 ± 0.13	1.00 ± 0.24	0.19 ± 0.04
	Error sqrt(A) (%)	10	10	10
	Error thickness (%)	10	10	10
	Error distal integration limit (%)	20	20	20

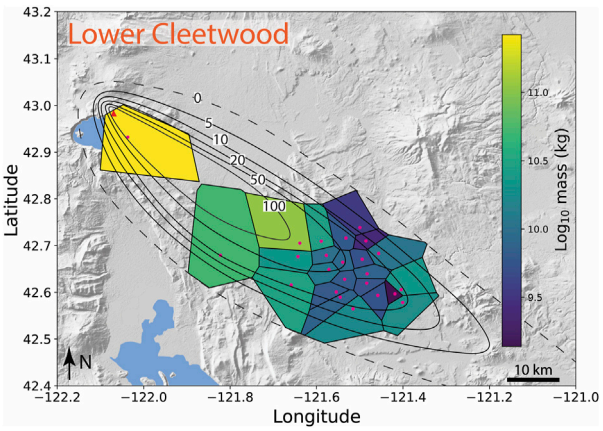

FIGURE 9 | Voronoi tessellation of lower Cleetwood of the Cleetwood eruptive sequence used to calculate the total grain-size distribution (TGSD). Pink dots indicate samples analyzed for their GSD via sieving and weighing. Isolines are in centimeters. Background is global Earth relief (Tozer et al., 2019).

increase in obsidian pyroclasts, which makes up to 23 vol.% of size fraction 0.125–0.25 mm. Young (1990), Bourgeois (1998), and Wearn (2002) all attributed this increase in obsidian pyroclasts towards the end of the Cleetwood eruption to the progressive annealing of juvenile glass to the conduit walls, which is then mostly eroded during this final explosive phase. Gardner et al. (2017) and Watkins et al. (2017) showed that obsidian pyroclasts from the North Mono Craters (CA, United States) formed by the syn-eruptive agglomeration and sintering of ash fragments on the conduit walls above the level of fragmentation, which were then remobilized over a wide range of depths and ejected together with juvenile porous pyroclasts. Wadsworth et al. (2019) showed that in the absence of a confining pressure, the timescale for sintering decreases with decreasing particle radius. We propose that ash fragments begin to sinter and weld to the conduit walls during Llao Rock and lower Cleetwood. As the MER wanes during lower Cleetwood, as evidenced by the strong normal grading of that phase, sintering and welding dominate over erosion and ejection. This continues until the end of lower Cleetwood and perhaps even partially seals the conduit (Wadsworth et al., 2019), which in turn repressurizes the system and may trigger upper Cleetwood. As the MER increases over the course of upper Cleetwood, erosion begins to dominate over agglomeration and sintering, leading to an increase in both obsidian pyroclasts and lithics in the deposit of upper Cleetwood. It should be noted that layer 5F (**Figures 5**, **7**), from which we determined componentry of upper Cleetwood, does not lie directly on the dispersal axis of upper Cleetwood and therefore probably represents minimum abundances of

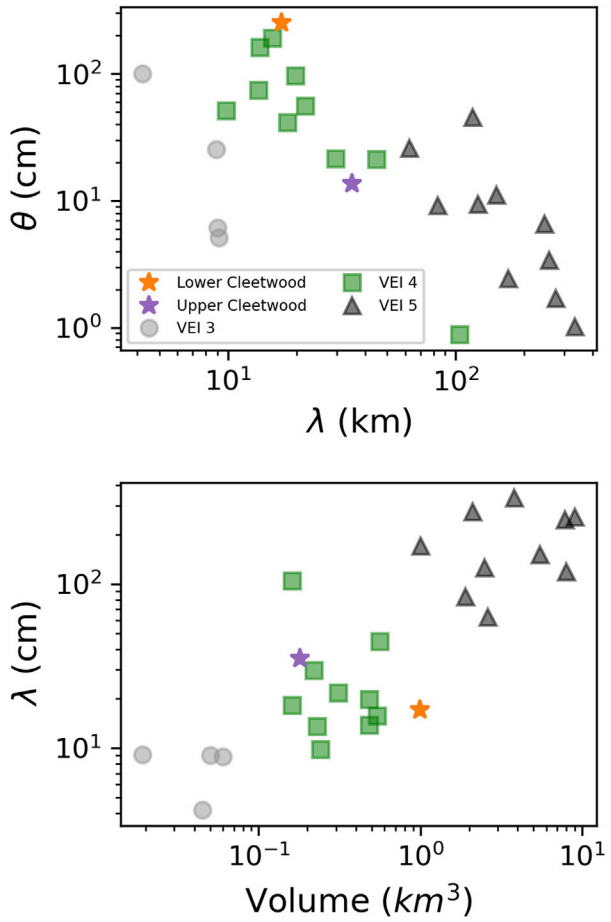

FIGURE 10 | Best fit Weibull parameters for the three phases of the Cleetwood eruptive sequence plotted together with VEI 3, VEI4, and VEI 5 eruptions compiled by Bonadonna and Costa (2012). **(A)** θ vs λ. **(B)** λ vs total erupted volume (non-DRE). In both graphs, note that all three phases of the Cleetwood eruptive sequence plot with other VEI 4 eruptions.

dense component (lithic, pyroclastic obsidian), when compared with those from Llao Rock and lower Cleetwood.

Judging solely from the contact between lower Cleetwood and upper Cleetwood, it is difficult to say whether these two phases correspond to two distinct plumes or if upper Cleetwood simply marks an increase in plume height and MER from the end of lower Cleetwood, due to vent widening. The thin grey ash layer making contact between lower Cleetwood and upper Cleetwood shows no visible signs of erosion. Thus, if a separate plume is responsible for the deposition of upper Cleetwood, it occurred shortly after the end of lower Cleetwood. Furthermore, this grey ash layer is only present at SE medial locations, which indicates that the dominant wind shifts from the SE to the ESE by the end upper Cleetwood, when plume height and MER were at a maximum.

Comparison With Modern Equivalents

Although there are many historic examples of highly silicic eruptions that transitioned from explosive to effusive activity within the same eruptive sequence (e.g., the 1060 CE Glass Mountain eruption of Medicine Lake volcano, California, United States, Heiken, 1978; the 700 CE Big Obsidian Flow eruption at Newberry Volcano, Oregon, United States, Kuehn, 2002), the rhyolitic eruptions of Chaitén (2008, Chile; Alfano et al., 2011) and Cordón Caulle (2011–2012, Chile; Pistolesi et al., 2015) provided the first real-time observations of an eruption of this type in modern history. The 2008 eruption of Chaiten consisted of a series of VEI 4 eruptions that began on May 1 with a ~0.5 km^3 explosive phase (Watt et al., 2009; Alfano et al., 2011; Durant et al., 2012) and climaxed on May 6th with a sub-Plinian eruption that ejected ~0.3 km^3 of tephra from a 19 ± 1 km high plume (Carn et al., 2009; Alfano et al., 2016), which corresponds to a MER of ~2.8 × 10^7 kg s^{-1} (Mastin, 2014). On May 11, the explosive activity began transitioning to effusive activity that eventually emplaced a ~0.8 km^3 rhyolitic flow (Pallister et al., 2013). The 2011–2012 eruption of Cordón Caulle can be divided into four explosive phases, two of which being classified as VEI 4 eruptions. The first and most intense sub-Plinian phase began on June 4 and deposited ~0.75 km^3 of tephra from a ~11–14 km plume and MER on the order of 10^7 kg s^{-1}. The second phase (5–6 June) fluctuated with MERs of 10^6–10^7 kg s^{-1} and deposited ~0.21 km^3 of material ending with the deposition of an obsidian-rich tephra layer. The third and fourth phases (June 7 and later) consisted of VEI 3 eruptions depositing a total of ~0.05 km^3 of tephra (Bonadonna et al., 2015; Pistolesi et al., 2015). Effusive activity began on June 15 from the same vent and produced a ~0.6 km^3 rhyolitic flow (Castro et al., 2013; Jay et al., 2014; Bertin et al., 2015). Calculated volumes, plume height, and MER for the Cleetwood eruptive sequence are like these two modern analogs, and we thus infer that the Cleetwood eruption unfolded in a manner and timing similar to that of these Chilean eruptions; explosive Llao Rock, lower Cleetwood, and upper Cleetwood all occurred within a period of days, followed, days/weeks later, by the emplacement of the rhyodacitic Cleetwood Flow from the same vent, perhaps interspersed by hybrid explosive-effusive activity (Schipper et al., 2013).

Grain-Size Distribution

TGSD of the Cleetwood Eruption

Exhaustive sample collection and grain-size data for the Cleetwood deposit are difficult to obtain due to the extreme thickness of the overlying Climactic deposit at proximal locations, and difficulties in distinguishing the Cleetwood from the Climactic deposits at distal locations. The TGSD of lower Cleetwood of the eruption, the only phase for which we believe we have enough data to calculate an accurate TGSD, was thus constructed using samples collected at 24 locations 6–72 km from the vent. All the points used to build the TGSD are within the 5 cm isoline (**Figure 9**) and, given the density of data obtained within this area, we believe the TGSD built using the Voronoi tessellation is representative of the material deposited within that 5 cm isoline. Using the Weibull model of Bonadonna and Costa (2012), the volume of deposit enclosed within the 5 cm isoline can be calculated using

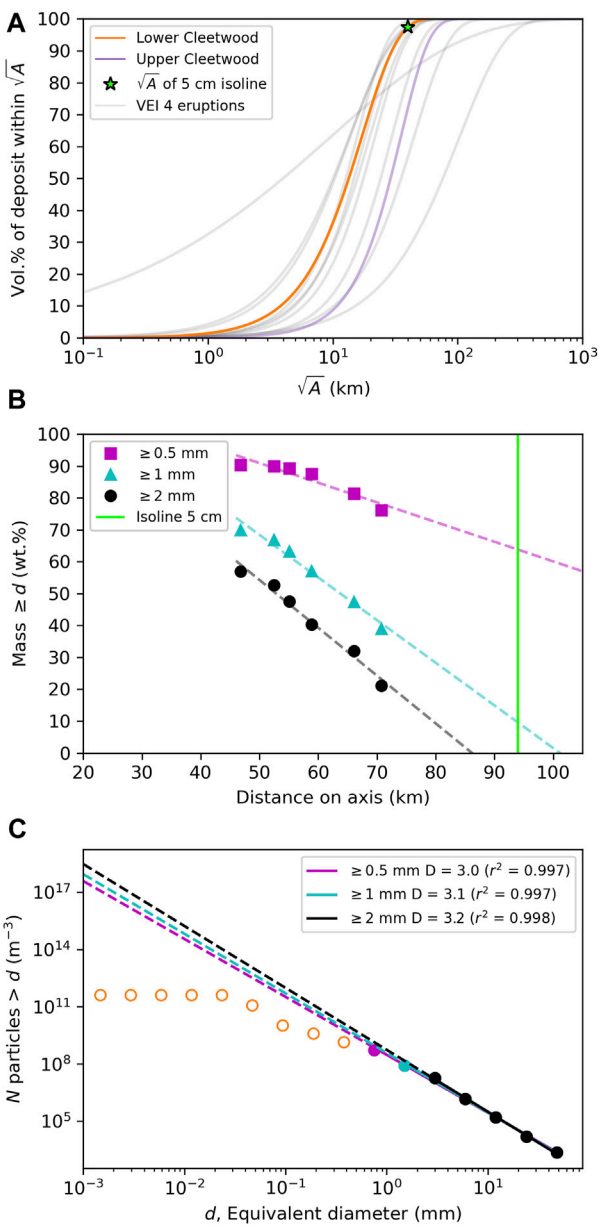

FIGURE 11 | (A) Cumulative volume of tephra of lower Cleetwood of the Cleetwood eruptive sequence as a function of the square root of the isopach area, $\sqrt{A}$ (km). Data for all other VEI 4 eruptions compiled by Bonadonna and Costa (2012) are also plotted, in gray, for comparison. **(B)** Mass fraction (in wt.%) of particles ≥0.5 mm, ≥1 mm, or ≥2 mm as a function of the distance from the vent along the dispersal axis of lower Cleetwood. The vertical green line represents the furthest extent of the 5 cm isoline (**Figure 4B**). Because all locations plotted lie on the dispersal axis, the mass ≥ *d* for each grain-size likely represents maximum values. **(C)** Cumulative number density, $N > d$, vs equivalent diameter, *d*, for lower Cleetwood of the Cleetwood eruption (i.e., TGSD) and best fits obtained using a power-law distribution for all particles ≥0.5 mm, ≥1 mm, and ≥2 mm. The fractal dimension and Pearson coefficient obtained for each case are given in the legend.

$$V(x) = \frac{2\theta\lambda^2}{n}\left[1 - e^{-(x/\lambda)^n}\right] \quad (1)$$

where x (km) is the square root of isopach area for isoline 5 cm, λ (km) is the characteristic decay length scale of deposit thinning, θ (cm) is a thickness scale, and n is a dimensionless shape parameter (λ, θ, and n are provided in **Table 2**). Using **Eq. 1**, the volume enclosed by the 5 cm isoline is ~0.97 km^3, corresponding to about 97% of the whole volume of tephra ejected during lower Cleetwood, consistent with other VEI 4 eruptions (**Figure 11A**). Furthermore, the proportions of pyroclasts ≥2 mm and ≥1 mm in samples of lower Cleetwood collected along the main dispersion axis decrease downwind and reach 0% and <10%, respectively, when extrapolated to where the isoline 5 cm crosses the main axis of dispersion (at ~94 km, **Figure 4B**, **Figure 11B**). We thus infer that the TGSD calculated for lower Cleetwood using medial data is representative of the whole TGSD for particles larger than ~1 mm. Over that range of sizes, the TGSD can be nicely fit using a power law distribution and a fractal dimension D = 3.1 (**Figure 11C**; D = 3.2 is obtained when fitting only particles ≥2 mm, and D = 3.0 for particles ≥0.5 mm).

In the absence of distal data in this study, it is impossible to accurately construct the TGSD for lower Cleetwood of the Cleetwood eruption for particles ≤ 1 mm. However, compilations of TGSDs of >20 sub-Plinian and Plinian eruptions show that all can be fit using a single power law distribution over the whole range of particle sizes (~10^{-3}–10^3 mm), with a fractal dimension D ≥ 3 (see compilations in Kaminski and Jaupart, 1998; Rust and Cashman, 2011). In particular, eruptions of silicic magma with MER similar to lower Cleetwood of the Cleetwood eruption and ranging from 1.5 × 10^7 kg s^{-1} to 7.9 × 10^7 kg s^{-1} (MER for lower Cleetwood is 3.1 × 10^7 kg s^{-1}) have D values close to 3 (e.g., Phase D Askja 1875: D = 3.0, Kaminski and Jaupart 1998; Unit B 79 cal CE Mt. Pelée: D = 3.0, Carazzo et al., 2020; Mt. St. Helens, 18 May 1980: D = 3.1, Rust and Cashman, 2011; Layer β 2008 Chaitén: D = 3.0, Alfano et al., 2016). Given these observations, we speculate that the TGSD of lower Cleetwood can be fit using a power law with a fractal dimension of ~3.1 over the whole range of particles sizes. As shown below, in the absence of distal data to construct the TGSD, we believe that individual high-resolution GSDs at medial locations on the dispersal axis can provide further insight into the fractal dimension of an eruption's TGSD.

High-Resolution GSDs

The high-resolution GSDs produced for individual locations do not equate to the whole TGSD of the deposit as they partly reflect transport processes (Pioli et al., 2019). Despite this, important information can still be gleaned from these individual GSDs. As seen in the results section above, all high-resolution GSDs in this study, regardless of the eruptive phase or sample location, show two systematic breaks in slope from a power-law relationship at ~0.125 and ~0.510 mm. These breaks in slope create three

individual segments S1 (particles<0.125 mm), S2 (particles 0.125–0.510 mm), and S3 (particles >0.510 mm) that can all be fit by a power-law relationship with fractal dimensions *D1*, *D2*, and *D3*, respectively. We discuss below the signification of each of these segments.

Particles <0.125 mm–Inheritance From Primary Fragmentation

Values of *D1* (**Table 2**; **Supplementary Table 3**) are 2.5 ± 0.2 regardless of eruptive phase, distance from the vent, and location with respect to the dispersal axis. These values are within the range of those obtained by rapid decompression experiments (Kueppers et al., 2006). Particles are predominantly juvenile ash over the range of sizes covered by S1 (**Figures 6**, **7**), and thus the fractal dimension at these sizes is largely controlled by the size distribution of this component. Jones and Russell (2017) conducted pumice attrition experiments at varying time lengths and showed that a time ≥30 min was necessary to change the slope of the GSD for particles <0.156 mm, approximately equal to our S1 range. This timescale is far too long to represent transit time within the conduit after fragmentation (estimated to be of the order of 10^1–10^2 s for Plinian eruptions; Gardner et al., 1996), and Jones and Russell (2017) suggested that their longer experimental runs could represent residence times in the plume. However, the bulk ash concentration used in their experiments is ~4,000 g m^{-3}, whereas measured concentrations in real plumes are three orders of magnitude lower (e.g., 3.6–4.9 g m^{-3} for the 1980 eruption of Mt. St. Helens; Harris and Rose, 1983). This suggests that the size distribution of particles within this size range only evolves slightly after initial magma fragmentation.

Giachetti et al. (2021) showed that some pumice lapilli from sub-Plinian and Plinian eruptions, including the Cleetwood eruption, are pumice agglomerates comprised of protopyroclasts, the products of primary magma fragmentation. These pumice aggregates are created by the agglomeration and partial sintering of protopyroclasts of all sizes as they collide during ascent in the conduit seconds after initial magma fragmentation. Giachetti et al. (2021) showed that the size distributions of 0.001–10-mm protopyroclasts from two sub-Plinian rhyolitic eruptions, the 1060 CE Glass Mountain eruption of Medicine Lake volcano (California, United States; Heiken, 1978) and the 700 CE Big Obsidian Flow eruption at Newberry Volcano (Oregon, United States; Kuehn, 2002), are power-law with *D* values of 2.5 ± 0.1. These power-law exponents are consistent with those of the products of experimental magma fragmentation by rapid decompression (Kueppers et al., 2006). The *D1* values found in our study are also in the same range. Using the methodology developed by Giachetti et al. (2021), we analyzed the size distribution of protopyroclasts 1.5–30 μm in a pumice from the onset of lower Cleetwood, collected at location Cltwd 5 (layer 5D, see **Figure 5**). Protopyroclasts were only analyzed for this narrow size range because outlining individual clasts at larger sizes in these Cleetwood pumices becomes too subjective. Indeed, Giachetti et al. (2021) suggested that the fluidization of packed beds of protopyroclasts immediately after fragmentation could be more efficient for eruptions with MERs >10^7 kg s^{-1} (e.g., lower Cleetwood of the Cleetwood eruption), leaving less time for the mixing and amalgamation of protopyroclasts with highly contrasting textures, and thus making the boundaries between protopyroclasts less visually apparent. The size distribution of 3,011 protopyroclasts 1.5–30 μm in size analyzed in the pumice lapillus of lower Cleetwood is best fit by a power-law with a *D* value of 2.7. Interestingly, the GSD of lower Cleetwood is best fit by a power-law with *D1* = 2.6 for particles <0.125 mm (**Table 1**).

Although further investigation is necessary, our results suggest that the fractal dimension of the GSD of particles <0.125 mm collected at medial locations on the dispersal axis of explosive deposits reflects the size distribution of the primary products of magma fragmentation in the conduit (i.e., like the distribution of protopyroclasts within pumice aggregates; Giachetti et al., 2021), and thus could be used to infer the potential energy at fragmentation. This hypothesis is supported by the fact that, at a given location, there is a positive correlation between the value of *D1* and the median grain-size, and thus the MER (**Figure 12**).

Particles 0.125–0.510 mm–Clues for Rafting During Transport

The second portion of the individual GSDs, S2 (particles 0.125–0.510 mm), can also be fit with a power-law giving D2 values of 0.6 ± 0.1. This fractal dimension does not vary systematically with explosive phase, distance from the vent, nor location with respect to the dispersal axis (**Table 1**). This size fraction shows a noticeably higher proportion of non-juvenile components (i.e., loose crystals and lithics) compared to S1 and S3 (**Figure 7**). These components are not the primary products of fragmentation and thus this enrichment could be a contributing factor to where and why this break in slope with S1 occurs. A recent theoretical study also suggests that particle rafting can modify the way in which some particles locally sediment (Rossi et al., 2021). Rafting occurs when fine particles aggregate around a relatively dense core particle during transport. The resulting aggregate has a density significantly lower than its core due to the air entrapped in between aggregating particles. This leads to relatively dense particles "rafting" and landing further than where they would have if smaller particles had not aggregated around them. Upon impact and over time these aggregates break apart and are rarely found intact when sampling historic eruptions. In their theoretical framework, Rossi et al. (2021) defined the size range of core particles that could undergo rafting as 0.138–0.710 mm, which mostly overlaps with the range of sizes over which we see major changes in the shape of our GSDs. Note that this transport process changes the individual GSDs at some locations, but not the overall TGSD of the eruption.

To investigate whether particle rafting may have occurred during the Cleetwood eruption and if this process can explain part of the shape of our GSDs, we analyzed the size distribution of the porous (pumice and banded pumice) and dense (obsidian pyroclasts, lithics, and loose crystals) components of a single layer at increasing distance from the vent, along the main axis of

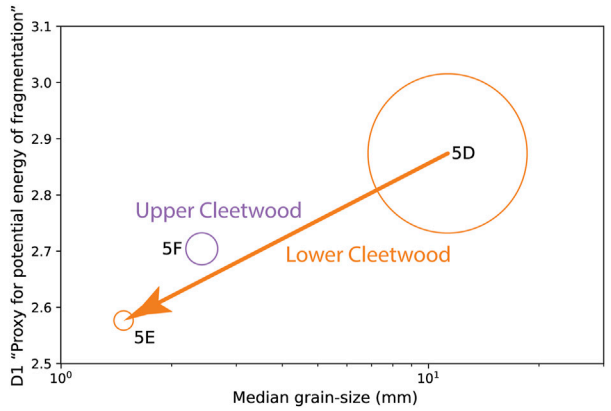

FIGURE 12 | D1 values (i.e., fractal dimension of the cumulative size distribution of particles <0.125 mm) found for all subunits of Cltwd 5, plotted as a function of the median grain-size of that subunit. Circle size is representative of the inferred plume height and thus mass eruption rate (MER), being the lowest for Llao Rock, highest but continuously decreasing (from 5D to 5E) for lower Cleetwood, and intermediate for upper Cleetwood.

dispersion. Layers 5E, 17D, 18B (**Figure 5**) all correspond to the end of lower Cleetwood and are located on the main dispersal axis at 46 km, 56 km, and 66 km from the proposed vent location, respectively. All three locations show an unexpected increase in particle number density over the size range ~0.125–0.650 mm (**Figure 13A**), which is not related to data combination as the same observation is made using laser diffraction data alone (see inset in **Figure 13A**). As expected, the overall median grain-size decreases with distance from the vent as the GSDs of 5E, 17D, and 18B skew towards finer particle sizes due to density sorting during transport in the plume (**Figures 13B–D**). However, the componentry (realized on sieved fractions independently of laser diffraction and DIA analyses), shows that the proportion of dense particles that compose the size fraction in which we see an increase in particle number density simultaneously increases from 4% at 46 km from the vent, to 18% at 56 km, and finally to 34% at 66 km (i.e., from Cltwd 5, Cltwd 17 to Cltwd 18, respectively, **Figures 13B–D**). Furthermore, this increase in the volume percent of dense components is accompanied by an increase in the median grain-size of the dense particles as a function of distance, from ~0.27 mm at Cltwd 5 to ~0.31–0.33 mm at Cltwd 17 and 18, which is not expected (**Figure 13E**). We infer that this increase in both the proportion and the median grain-size of dense particles with distance from the vent are clues that particle rafting delayed their sedimentation (Rossi et al., 2021).

Particles >0.510 mm–Influence of Sedimentation

This portion of the GSD, which corresponds to particles >0.510 mm, is predominantly composed of juvenile pumice (**Figure 7**). For all layers of all phases, it can be nicely fit with a power-law equation with a fractal dimension *D3* between 2.7 and 4.7. For a given phase, the value of D3 increases with distance from the vent along the main dispersion axis, testifying to a progressive loss of larger particles. For example, for lower Cleetwood, *D3* is equal to 2.95 at ~46 km

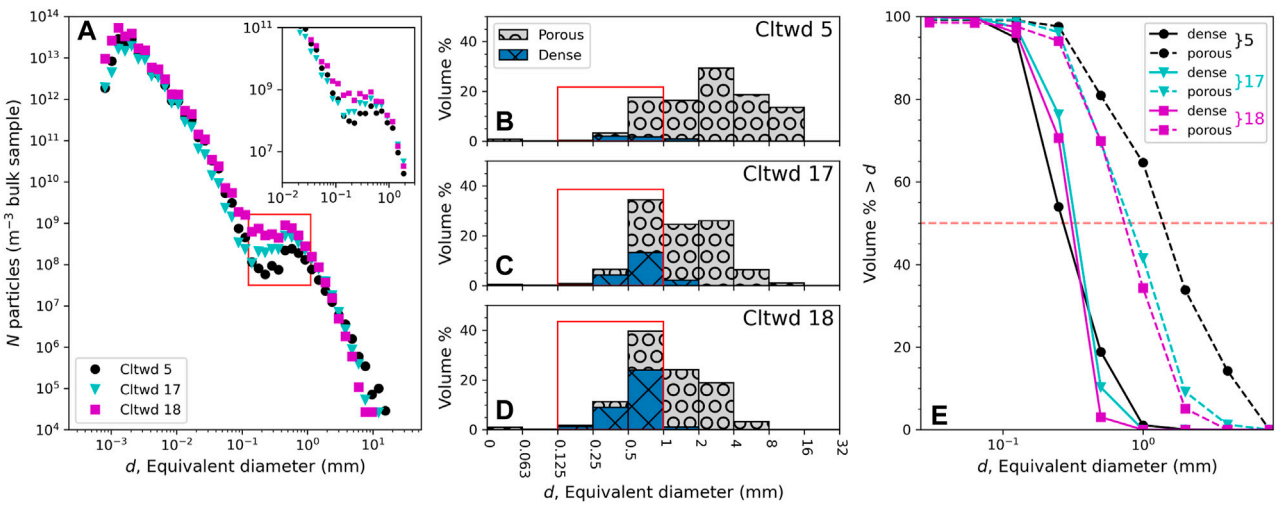

FIGURE 13 | (A) Number density, *N*, vs equivalent diameter, *d*, for the end of lower Cleetwood at locations Cltwd 5, 17, and 18, which are all located on the main dispersal axis at 46 km, 56 km, and 66 km from the proposed vent location, respectively. Note the sudden increase in number density of particle for ~0.1 mm < *d* < ~1 mm (red rectangle). Inset shows *N* vs *d* using laser diffraction data only and further illustrate that this increase is not an artifact of merging datasets (see also **Figure 3B**). **(B-D)** Volume percent of porous and dense material vs *d* for locations Cltwd 5, 17, and 18, respectively. Note the increase of the proportion of dense particles in size range 0.125–1 mm with increasing distance from the vent (red rectangles). **(E)** Cumulative volume distribution for porous (dashed lines) and dense (solid lines) material at Cltwd 5, 17, and 18. Median grain-sizes are at the intersections of these distributions with a volume percent of 50% (i.e., horizontal red dashed line). Note the slight increase in the median diameter of dense particles from Cltwd 5 to Cltwd 17 and 18, which we attribute to particle rafting, whereas the median diameter of the porous particles logically decreases with increasing distance from the vent.

from the vent (Cltwd 5), increasing to 3.10 at ~56 km (Cltwd 17), and to 3.32 at ~66 km (Cltwd 18). At these three locations, particles ≥0.5 mm (approximately the lower bound of *D3*) represent >80% of the mass of the sample, and it is thus not surprising that these *D3* values (~3.1 ± 0.2) are close to the fractal dimension of the calculated TGSD for particles >0.5 mm (3.0, see **Figure 11C**).

CONCLUSION

The successful modeling and forecasting of the dispersion and sedimentation of tephra from explosive volcanic eruptions rely heavily on the initial eruption source parameters inputs such as plume height, erupted volume, MER and Total Grain-Size Distribution. During an eruption, these parameters are challenging to determine and depend on those derived from detailed field studies of similar historic events. Here we calculated eruption source parameters for the ~7.7 ka Cleetwood eruption of Mount Mazama (Crater Lake/giiwas, Oregon, United States). We applied a novel approach to produce high-resolution grain-size distributions over the range 0.00035–35 mm by combining laser diffraction and dynamic image analysis techniques.

The ~7.7 ka Cleetwood eruptive sequence of Mount Mazama consisted of three consecutive rhyodacitic VEI 4 eruptions: Llao Rock, lower Cleetwood, and upper Cleetwood, from oldest to youngest. Lower Cleetwood was the most intense (Ht = ~19 km; MER = ~3.1×10^7 kg s^{-1}) and voluminous (~0.98 km^3) of the sequence with a TGSD that can be fit with a fractal dimension of ~3.1. Altogether, the Cleetwood eruption deposited 1.44 km^3 (non-DRE) of tephra from at least two, but no more than three, separate plumes. Explosive activity then transitioned to an effusive stage, with no apparent break, extruding a rhyodacitic lava flow with a minimum volume of ~0.6 km^3. The continuity and deposit of the Cleetwood eruption of Mount Mazama is similar to the only two witnessed volcanic eruptions of rhyolitic magma that transition to an effusive phase: Chaitén (Chile, 2008; fall = ~1 km^3, flow = ~0.8 km^3, plume height = ~19 km) and Cordón Caulle (Chile, 2011–2012; fall = ~0.8 km^3, flow = ~0.8 km^3, plume height = ~14 km). Further detailed fieldwork in proximal deposits of the latter upper Cleetwood of the Cleetwood eruption would be necessary to resolve whether there was coeval (hybrid) effusive and explosive activity as suggested by observations at Cordón Caulle during the 2011–2012 eruption.

Regardless of the eruptive phase or sample location, all high-resolution cumulative GSDs show two systematic breaks in slope from a power-law relationship at ~0.125 and ~0.510 mm, creating three individual segments that can all be fit by power-law relationships. We show that in conjunction with eruption source parameters and detailed componentry, our high-resolution GSDs provide insight into magma fragmentation and tephra transport. We show that the fractal dimension for particles <0.125 mm from medial locations on the dispersal axis of the tephra deposit reflects the size distribution of the primary products of magma fragmentation, and thus could be used to infer the potential energy at fragmentation. This observation is further supported by the positive correlation between the D1 value and the median grain-size at a given location. The overall low slope of the GSD for particles 0.125–0.510 mm is due to an increase in the amount of dense components (obsidian pyroclasts, lithics, and loose crystals) that is accompanied by an increase in their median grain-size with distance. We infer that this is due to particle rafting and thus delayed sedimentation. Lastly, the increasing slope of the GSDs for particles >0.510 mm with increasing distance from the vent, reflects the progressive and rather rapid loss of coarse ash and lapilli in the medial portion of the deposit. Our comparison of high-resolution GSDs across a fallout deposit has potential for identifying processes that modify tephra dispersal and sedimentation, such as particle rafting. Newly gleaned information using a higher resolution of GSDs would greatly further our understanding of both primary and secondary eruptive processes and help constrain eruption modeling and hazard assessment in the future.

PERMISSION TO REUSE AND COPYRIGHT

DATA AVAILABILITY STATEMENT

The datasets presented in this study can be found in online repositories. The names of the repository/repositories and accession number(s) can be found below: https://doi.org/10.5281/zenodo.5874666.

AUTHOR CONTRIBUTIONS

JW performed grain-size analysis, componentry, and wrote the first draft of the manuscript. JW and TG collaborated in conceiving this study, collecting samples, developing conceptual models, analyzing protopyroclasts, and drafting the final version of this manuscript.

FUNDING

JW and TG were partly funded by the National Science Foundation grant EAR-1725207. JW would like to thank the Jack Kleinman Memorial Fund for Volcano Research for their grant that helped carrying out the field work.

ACKNOWLEDGMENTS

We thank Sebastien Biass and Fabio Dioguardi for their detailed review of the manuscript and the Editor Antonio Costa for the swift handling of our paper. We also thank C. McDermott for her time as our archeological monitor and keeping us updated with wildfire movement while working in the Fremont-Winema National Forest. We are grateful to J.E. Gardner, K.R. Trafton, and J.M. Watkins for their help in the field. Thanks to A.R. Van Eaton, L.G. Mastin, and H.M.N. Wright for their time and help during laser diffraction analysis at the Cascades Volcano Observatory. We also thank C.R. Bacon for the insightful discussions about Mount Mazama.

SUPPLEMENTARY MATERIAL

The Supplementary Material for this article can be found online at: https://www.frontiersin.org/articles/10.3389/feart.2022.853021/full#supplementary-material

REFERENCES

Alfano, F., Bonadonna, C., Volentik, A. C. M., Connor, C. B., Watt, S. F. L., Pyle, D. M., et al. (2011). Tephra Stratigraphy and Eruptive Volume of the May, 2008, Chaitén Eruption, Chile. *Bull. Volcanol* 73 (5), 613–630. doi:10.1007/s00445-010-0428-x

Alfano, F., Bonadonna, C., Watt, S., Connor, C., Volentik, A., and Pyle, D. M. (2016). Reconstruction of Total Grain Size Distribution of the Climactic Phase of a Long-Lasting Eruption: the Example of the 2008–2013 Chaitén Eruption. *Bull. Volcanology* 78 (7), 1–21. doi:10.1007/s00445-016-1040-5

Bacon, C. R. (1983). Eruptive History of Mount Mazama and Crater Lake Caldera, Cascade Range, U.S.A. *J. Volcanology Geothermal Res.* 18 (1–4), 57–115. doi:10.1016/0377-0273(83)90004-5

Bacon, C. R., Gardner, J. V., Mayer, L. A., Buktenica, M. W., Dartnell, P., Ramsey, D. W., et al. (2002). Morphology, Volcanism, and Mass Wasting in Crater Lake, Oregon. *Bull. Geol. Soc. America* 114 (6), 675–692. doi:10.1130/0016-7606(2002)114<0675:mvamwi>2.0.co;2

Bacon, C. R., and Lanphere, M. A. (2006). Eruptive History and Geochronology of Mount Mazama and the Crater Lake Region, Oregon. *Geol. Soc. America Bull.* 118 (11–12), 1331–1359. doi:10.1130/B25906.1

Bertin, D., Lara, L. E., Basualto, D., Amigo, Á., Cardona, C., Franco, L., et al. (2015). High Effusion Rates of the Cordón Caulle 2011-2012 Eruption (Southern Andes) and Their Relation with the Quasi-Harmonic Tremor. *Geophys. Res. Lett.* 42 (17), 7054–7063. doi:10.1002/2015gl064624

Biass, S., Bonadonna, C., and Houghton, B. F. (2019). A Step-by-step Evaluation of Empirical Methods to Quantify Eruption Source Parameters from Tephra-Fall Deposits. *J. Appl. Volcanol.* 8 (1), 1. doi:10.1186/s13617-018-0081-1

Biass, S., Bagheri, G., Aeberhard, W., and Bonadonna, C. (2014). TError: towards a Better Quantification of the Uncertainty Propagated during the Characterization of Tephra Deposits. *Stat. Volcanology* 1 (2), 1–27.

Blott, S. J., and Pye, K. (2006). Particle Size Distribution Analysis of Sand-Sized Particles by Laser Diffraction: An Experimental Investigation of Instrument Sensitivity and the Effects of Particle Shape. *Sedimentology* 53 (3), 671–685. doi:10.1111/j.1365-3091.2006.00786.x

Bonadonna, C., Cioni, R., Pistolesi, M., Elissondo, M., and Baumann, V. (2015). Sedimentation of Long-Lasting Wind-Affected Volcanic Plumes: the Example of the 2011 Rhyolitic Cordón Caulle Eruption, Chile. *Bull. Volcanology* 77 (2), 1–19. doi:10.1007/s00445-015-0900-8

Bonadonna, C., Connor, C. B., Houghton, B. F., Connor, L., Byrne, M., Laing, A., et al. (2005). Probabilistic Modeling of Tephra Dispersal: Hazard Assessment of a Multiphase Rhyolitic Eruption at Tarawera, New Zealand. *J. Geophys. Res.*, 110(B3). doi:10.1029/2003JB002896

Bonadonna, C., and Costa, A. (2012). Estimating the Volume of Tephra Deposits: A New Simple Strategy. *Geology* 40 (5), 415–418. doi:10.1130/G32769.1

Bonadonna, C., and Costa, A. (2013). Plume Height, Volume, and Classification of Explosive Volcanic Eruptions Based on the Weibull Function. *Bull. Volcanol* 75 (8), 1–19. doi:10.1007/s00445-013-0742-1

Bonadonna, C., and Houghton, B. F. (2005). Total Grain-Size Distribution and Volume of Tephra-Fall Deposits. *Bull. Volcanol* 67 (5), 441–456. doi:10.1007/s00445-004-0386-2

Bonadonna, C., and Phillips, J. C. (2003). Sedimentation from strong Volcanic Plumes. *J. Geophys. Res. Solid Earth* 108 (B7). doi:10.1029/2002jb002034

Bourgeois, R. L. (1998). *Physical Characteristics of Proximal Cleetwood Airfall Deposits, Crater Lake, OR: The Transition from Explosive to Effusive Eruption*. University of Oregon.

Buckland, H. M., Cashman, K. V., Engwell, S. L., and Rust, A. C. (2020). Sources of Uncertainty in the Mazama Isopachs and the Implications for Interpreting Distal Tephra Deposits from Large Magnitude Eruptions. *Bull. Volcanol* 82 (3), 23. doi:10.1007/s00445-020-1362-1

Buckland, H. M., Saxby, J., Roche, M., Meredith, P., Rust, A. C., Cashman, K. V., et al. (2021). Measuring the Size of Non-spherical Particles and the Implications for Grain Size Analysis in Volcanology. *J. Volcanology Geothermal Res.*, 415, 107257. doi:10.1016/j.jvolgeores.2021.107257

Carazzo, G., Tait, S., Michaud-Dubuy, A., Fries, A., and Kaminski, E. (2020). Transition from Stable Column to Partial Collapse during the 79 Cal CE P3 Plinian Eruption of Mt. Pelée Volcano (Lesser Antilles). *J. Volcanology Geothermal Res.*, 392, 106764. doi:10.1016/j.jvolgeores.2019.106764

Carey, S. N., and Sigurdsson, H. (1982). Influence of Particle Aggregation on Deposition of Distal Tephra from the MAy 18, 1980, Eruption of Mount St. Helens Volcano. *J. Geophys. Res.*, 87(B8), 7061–7072. doi:10.1029/JB087iB08p07061

Carey, S., and Sigurdsson, H. (1989). The Intensity of Plinian Eruptions. *Bull. Volcanol* 51 (1), 28–40. doi:10.1007/BF01086759

Carey, S., and Sparks, R. S. J. (1986). Quantitative Models of the Fallout and Dispersal of Tephra from Volcanic Eruption Columns. *Bull. Volcanology* 48 (2), 109–125. doi:10.1007/bf01046546

Carn, S. A., Pallister, J. S., Lara, L., Ewert, J. W., Watt, S., Prata, A. J., et al. (2009). The Unexpected Awakening of Chaitén Volcano, Chile. *Eos Trans. AGU* 90 (24), 205–206. doi:10.1029/2009eo240001

Castro, J. M., Schipper, C. I., Mueller, S. P., Militzer, A. S., Amigo, A., Parejas, C. S., et al. (2013). Storage and Eruption of Near-Liquidus Rhyolite Magma at Cordón Caulle, Chile. *Bull. Volcanology* 75 (4), 1–17. doi:10.1007/s00445-013-0702-9

Choumert-Nkolo, J., Lamour, A., and Phélinas, P. (2021). The Economics of Volcanoes. *EconDisCliCha* 5 (2), 277–299. doi:10.1007/s41885-021-00087-2

Costa, A., Pioli, L., and Bonadonna, C. (2016). Assessing Tephra Total Grain-Size Distribution: Insights from Field Data Analysis. *Earth Planet. Sci. Lett.*, 443, 90–107. doi:10.1016/j.epsl.2016.02.040

Dufek, J., and Manga, M. (2008). *In Situ* production of Ash in Pyroclastic Flows. *J. Geophys. Res.*, 113(B9). doi:10.1029/2007JB005555

Dufek, J., Manga, M., and Patel, A. (2012). Granular Disruption during Explosive Volcanic Eruptions. *Nat. Geosci* 5 (8), 561–564. doi:10.1038/ngeo1524

Durant, A. J., Villarosa, G., Rose, W. I., Delmelle, P., Prata, A. J., and Viramonte, J. G. (2012). Long-range Volcanic Ash Transport and Fallout during the 2008 Eruption of Chaitén Volcano, Chile. *Phys. Chem. Earth, Parts A/B/C* 45-46, 50–64. doi:10.1016/j.pce.2011.09.004

Egan, J., Staff, R., and Blackford, J. (2015). A High-Precision Age Estimate of the Holocene Plinian Eruption of Mount Mazama, Oregon, USA. *The Holocene* 25 (7), 1054–1067. doi:10.1177/0959683615576230

Engwell, S. L., Sparks, R. S. J., and Aspinall, W. P. (2013). Quantifying Uncertainties in the Measurement of Tephra Fall Thickness. *J. Appl. Volcanology* 2 (1), 1–12. doi:10.1186/2191-5040-2-5

Fierstein, J., and Nathenson, M. (1992). Another Look at the Calculation of Fallout Tephra Volumes. *Bull. Volcanol* 54 (2), 156–167. doi:10.1007/bf00278005

Folch, A., Mingari, L., Gutierrez, N., Hanzich, M., Macedonio, G., and Costa, A. (2020). FALL3D-8.0: a Computational Model for Atmospheric Transport and

Deposition of Particles, Aerosols and Radionuclides - Part 1: Model Physics and Numerics. *Geosci. Model. Dev.* 13 (3), 1431–1458. doi:10.5194/gmd-13-1431-2020

Gardner, J. E., Llewellin, E. W., Watkins, J. M., and Befus, K. S. (2017). Formation of Obsidian Pyroclasts by Sintering of Ash Particles in the Volcanic Conduit. *Earth Planet. Sci. Lett.*, 459, 252–263. doi:10.1016/j.epsl.2016.11.037

Gardner, J. E., Thomas, R. M. E., Jaupart, C., and Tait, S. (1996). Fragmentation of Magma during Plinian Volcanic Eruptions. *Bull. Volcanol* 58 (2), 144–162. doi:10.1007/s004450050132

Giachetti, T., Trafton, K. R., Wiejaczka, J., Gardner, J. E., Watkins, J. M., Shea, T., et al. (2021). The Products of Primary Magma Fragmentation Finally Revealed by Pumice Agglomerates. *Geology* 49 (11), 1307–1311. doi:10.1130/G48902.1

Harris, D. M., and Rose, Jr., W. I. (1983). Estimating Particle Sizes, Concentrations, and Total Mass of Ash in Volcanic Clouds Using Weather Radar. *J. Geophys. Res.*, 88(C15), 10969–10983. doi:10.1029/JC088iC15p10969

Heiken, G. (1978). Plinian-type Eruptions in the medicine lake highland, california, and the Nature of the Underlying Magma. *J. Volcanology Geothermal Res.*, 4(3), 375–402. doi:10.1016/0377-0273(78)90023-9

Jay, J., Costa, F., Pritchard, M., Lara, L., Singer, B., and Herrin, J. (2014). Locating Magma Reservoirs Using InSAR and Petrology before and during the 2011-2012 Cordón Caulle Silicic Eruption. *Earth Planet. Sci. Lett.* 395, 254–266. doi:10.1016/j.epsl.2014.03.046

Jones, A., Thomson, D., Hort, M., and Devenish, B. (2007). "The U.K.," in *Met Office's Next-Generation Atmospheric Dispersion Model, NAME III BT - Air Pollution Modeling and its Application XVII*. Editors C. Borrego ,and A.-L. Norman (Boston, MA: Springer US).

Jones, T. J., and Russell, J. K. (2017). Ash Production by Attrition in Volcanic Conduits and Plumes. *Sci. Rep.* 7 (1), 5538. doi:10.1038/s41598-017-05450-6

Kamata, H., Suzuki-Kamata, K., and Bacon, C. R. (1993). Deformation of the Wineglass Welded Tuff and the Timing of Caldera Collapse at Crater Lake, Oregon. *J. Volcanology Geothermal Res.* 56 (3), 253–265. doi:10.1016/0377-0273(93)90019-N

Kaminski, E., and Jaupart, C. (1998). The Size Distribution of Pyroclasts and the Fragmentation Sequence in Explosive Volcanic Eruptions. *J. Geophys. Res.*, 103(B12), 29759–29779. doi:10.1029/98JB02795

Kanamitsu, M., Ebisuzaki, W., Woollen, J., Yang, S.-K., Hnilo, J. J., Fiorino, M., et al. (2002). NCEP-DOE AMIP-II Reanalysis (R-2). *Bull. Am. Meteorol. Soc.* 83 (11), 1631–1643. doi:10.1175/BAMS-83-11-163110.1175/bams-83-11-1631(2002)083<1631:nar>2.3.co;2

Klawonn, M., Houghton, B. F., Swanson, D. A., Fagents, S. A., Wessel, P., and Wolfe, C. J. (2014a). Constraining Explosive Volcanism: Subjective Choices during Estimates of Eruption Magnitude. *Bull. Volcanology* 76 (2), 1–6. doi:10.1007/s00445-013-0793-3

Klawonn, M., Houghton, B. F., Swanson, D. A., Fagents, S. A., Wessel, P., and Wolfe, C. J. (2014b). From Field Data to Volumes: Constraining Uncertainties in Pyroclastic Eruption Parameters. *Bull. Volcanology* 76 (7), 1–16. doi:10.1007/s00445-014-0839-1

Kueppers, U., Perugini, D., and Dingwell, D. (2006). "Explosive Energy" during Volcanic Eruptions from Fractal Analysis of Pyroclasts. *Earth Planet. Sci. Lett.* 248 (3–4), 800–807. doi:10.1016/j.epsl.2006.06.033

Kueppers, U., Putz, C., Spieler, O., and Dingwell, D. B. (2012). Abrasion in Pyroclastic Density Currents: Insights from Tumbling Experiments. *Phys. Chem. Earth, Parts A/B/C*45-46, 33–39. doi:10.1016/j.pce.2011.09.002

Le Pennec, J.-L., Ruiz, G. A., Ramón, P., Palacios, E., Mothes, P., and Yepes, H. (2012). Impact of Tephra Falls on Andean Communities: The Influences of Eruption Size and Weather Conditions during the 1999-2001 Activity of Tungurahua Volcano, Ecuador. *J. Volcanology Geothermal Res.* 217-218, 91–103. doi:10.1016/j.jvolgeores.2011.06.011

Liu, E. J., Cashman, K. V., and Rust, A. C. (2015). Optimising Shape Analysis to Quantify Volcanic Ash Morphology. *GeoResJ*, 8, 14–30. doi:10.1016/j.grj.2015.09.001

Mastin, L. G. (2014). Testing the Accuracy of a 1-D Volcanic Plume Model in Estimating Mass Eruption Rate. *J. Geophys. Res. Atmos.*, 119(5), 2474–2495. doi:10.1002/2013JD020604

McCormick, M. P., Thomason, L. W., and Trepte, C. R. (1995). Atmospheric Effects of the Mt Pinatubo Eruption. *Nature* 373 (6513), 399–404. doi:10.1038/373399a0

Mele, D., Costa, A., Dellino, P., Sulpizio, R., Dioguardi, F., Isaia, R., et al. (2020). Total Grain Size Distribution of Components of Fallout Deposits and Implications for Magma Fragmentation Mechanisms: Examples from Campi Flegrei Caldera (Italy). *Bull. Volcanol* 82 (4), 31. doi:10.1007/s00445-020-1368-8

Murrow, P. J., Rose, Jr., W. I., and Self, S. (1980). Determination of the Total Grain Size Distribution in a Vulcanian Eruption Column, and its Implications to Stratospheric Aerosol Perturbation. *Geophys. Res. Lett.*, 7(11), 893–896. doi:10.1029/GL007i011p00893

Pallister, J. S., Diefenbach, A. K., Burton, W. C., Muñoz, J., Griswold, J. P., Lara, L. E., et al. (2013). The Chaitén Rhyolite Lava Dome: Eruption Sequence, Lava Dome Volumes, Rapid Effusion Rates and Source of the Rhyolite Magma. *Andean Geology.* 40 (2), 277–294. doi:10.5027/andgeov40n2-a06

Parfitt, E. A. (1998). A Study of Clast Size Distribution, Ash Deposition and Fragmentation in a Hawaiian-Style Volcanic Eruption. *J. Volcanol. Geotherm. Res.* 84 (3–4), 197–208. doi:10.1016/S0377-0273(98)00042-0

Perugini, D., and Kueppers, U. (2012). Fractal Analysis of Experimentally Generated Pyroclasts: A Tool for Volcanic hazard Assessment. *Acta Geophys.* 60 (3), 682–698. doi:10.2478/s11600-012-0019-7

Pioli, L., Bonadonna, C., and Pistolesi, M. (2019). Reliability of Total Grain-Size Distribution of Tephra Deposits. *Sci. Rep.* 9 (1), 1–15. doi:10.1038/s41598-019-46125-8

Pistolesi, M., Cioni, R., Bonadonna, C., Elissondo, M., Baumann, V., Bertagnini, A., et al. (2015). Complex Dynamics of Small-Moderate Volcanic Events: the Example of the 2011 Rhyolitic Cordón Caulle Eruption, Chile. *Bull. Volcanology* 77 (1), 1–24. doi:10.1007/s00445-014-0898-3

Pyle, D. M. (1989). The Thickness, Volume and Grainsize of Tephra Fall Deposits. *Bull. Volcanol* 51 (1), 1–15. doi:10.1007/BF01086757

Riley, C. M., Rose, W. I., and Bluth, G. J. S. (2003). Quantitative Shape Measurements of Distal Volcanic Ash. *J. Geophys. Res.*, 108(B10). doi:10.1029/2001JB000818

Robock, A. (2000). Volcanic Eruptions and Climate. *Rev. Geophys.*, 38(2), 191–219. doi:10.1029/1998RG000054

Rose, W. I., and Durant, A. J. (2011). Fate of Volcanic Ash: Aggregation and Fallout. *Geology* 39 (9), 895–896. doi:10.1130/focus092011.1

Rosi, M., Vezzoli, L., Castelmenzano, A., and Grieco, G. (1999). Plinian Pumice Fall deposit of the Campanian Ignimbrite Eruption (Phlegraean Fields, Italy). *J. Volcanology Geothermal Res.*, 91(2), 179–198. doi:10.1016/S0377-0273(99)00035-9

Rossi, E., Bagheri, G., Beckett, F., and Bonadonna, C. (2021). The Fate of Volcanic Ash: Premature or Delayed Sedimentation? *Nat. Commun.* 12 (1), 1303. doi:10.1038/s41467-021-21568-8

Rossi, E., Bonadonna, C., and Degruyter, W. (2019). A New Strategy for the Estimation of Plume Height from Clast Dispersal in Various Atmospheric and Eruptive Conditions. *Earth Planet. Sci. Lett.* 505, 1–12. doi:10.1016/j.epsl.2018.10.007

Rust, A. C., and Cashman, K. V. (2011). Permeability Controls on Expansion and Size Distributions of Pyroclasts. *J. Geophys. Res.*, 116(B11, a, n). doi:10.1029/2011JB008494

Saxby, J., Beckett, F., Cashman, K., Rust, A., and Tennant, E. (2018). The Impact of Particle Shape on Fall Velocity: Implications for Volcanic Ash Dispersion Modelling. *J. Volcanology Geothermal Res.*, 362, 32–48. doi:10.1016/j.jvolgeores.2018.08.006

Saxby, J., Rust, A., Beckett, F., Cashman, K., and Rodger, H. (2020). Estimating the 3D Shape of Volcanic Ash to Better Understand Sedimentation Processes and Improve Atmospheric Dispersion Modelling. *Earth Planet. Sci. Lett.*, 534, 116075. doi:10.1016/j.epsl.2020.116075

Schindelin, J., Arganda-Carreras, I., Frise, E., Kaynig, V., Longair, M., Pietzsch, T., et al. (2012). Fiji: an Open-Source Platform for Biological-Image Analysis. *Nat. Methods* 9 (7), 676–682. doi:10.1038/nmeth.2019

Schipper, C. I., Castro, J. M., Tuffen, H., James, M. R., and How, P. (2013). Shallow Vent Architecture during Hybrid Explosive-Effusive Activity at Cordón Caulle (Chile, 2011-12): Evidence from Direct Observations and Pyroclast Textures. *J. Volcanology Geothermal Res.* 262, 25–37. doi:10.1016/j.jvolgeores.2013.06.005

Schwaiger, H. F., Denlinger, R. P., and Mastin, L. G. (2012). Ash3d: A Finite-Volume, Conservative Numerical Model for Ash Transport and Tephra Deposition. *J. Geophys. Res.*, 117(B4, a, n). doi:10.1029/2011JB008968

Sigl, M., Winstrup, M., McConnell, J. R., Welten, K. C., Plunkett, G., Ludlow, F., et al. (2015). Timing and Climate Forcing of Volcanic Eruptions for the Past 2,500 Years. *Nature* 523 (7562), 543–549. doi:10.1038/nature14565

Sparks, R. S. J., Wilson, L., Sigurdsson, H., and Walker, G. P. L. (1981). The Pyroclastic Deposits of the 1875 Eruption of Askja, Iceland. *Phil. Trans. R. Soc. Lond. A.* 299 (1447), 241–273. doi:10.1098/rsta.1981.0023

Tozer, B., Sandwell, D. T., Smith, W. H. F., Olson, C., Beale, J. R., and Wessel, P. (2019). Global Bathymetry and Topography at 15 Arc Sec: SRTM15+. *Earth Space Sci.*, 6(10), 1847–1864. doi:10.1029/2019EA000658

Trafton, K. R., and Giachetti, T. (2021). The Morphology and Texture of Plinian Pyroclasts Reflect Their Lateral Sourcing in the Conduit. *Earth Planet. Sci. Lett.*, 562, 116844. doi:10.1016/j.epsl.2021.116844

Turcotte, D. L. (1997,). *Fractals and Chaos in Geology and Geophysics* (2nd ed.). doi:10.1017/CBO9781139174695

Turcotte, D. L. (1992). Fractals, Chaos, Self-Organized Criticality and Tectonics. *Terra Nova*, 4(1), 4–12. doi:10.1111/j.1365-3121.1992.tb00444.x

Wadsworth, F. B., Vasseur, J., Schauroth, J., Llewellin, E. W., Dobson, K. J., Havard, T., et al. 2019). A General Model for Welding of Ash Particles in Volcanic Systems Validated Using *In Situ* X-ray Tomography. *Earth Planet. Sci. Lett.*, 525, 115726. doi:10.1016/j.epsl.2019.115726

Walker, G. P. L. (1981b). Characteristics of Two Phreatoplinian Ashes, and Their Water-Flushed Origin. *J. Volcanology Geothermal Res.*, 9(4), 395–407. doi:10.1016/0377-0273(81)90046-9

Walker, G. P. L. (1980). The Taupo Pumice: Product of the Most Powerful Known (Ultraplinian) Eruption? *J. Volcanology Geothermal Res.*, 8(1), 69–94. doi:10.1016/0377-0273(80)90008-6

Walker, G. P. L. (1981a). The Waimihia and Hatepe Plinian Deposits from the Rhyolitic Taupo Volcanic Centre. *New Zealand J. Geology. Geophys.* 24 (3), 305–324. doi:10.1080/00288306.1981.10422722

Watkins, J. M., Gardner, J. E., and Befus, K. S. (2017). Nonequilibrium Degassing, Regassing, and Vapor Fluxing in Magmatic Feeder Systems. *Geology* 45 (2), 183–186. doi:10.1130/G38501.1

Watt, S. F. L., Pyle, D. M., Mather, T. A., Martin, R. S., and Matthews, N. E. (2009). Fallout and Distribution of Volcanic Ash over Argentina Following the May 2008 Explosive Eruption of Chaitén, Chile. *J. Geophys. Res. Solid Earth* 114 (B4). doi:10.1029/2008jb006219

Wearn, K. M. (2002). *Pyroclastic Obsidian from the Cleetwood and Rock Mesa Eruptions, Central Oregon*. University of Oregon.

Wilson, L., Sparks, R. S. J., and Walker, G. P. L. (1980). Explosive Volcanic Eruptions - IV. The Control of Magma Properties and Conduit Geometry on Eruption Column Behaviour. *Geophys. J. Int.*, 63(1), 117–148. doi:10.1111/j.1365-246X.1980.tb02613.x

Young, S. R. (1990). *Physical Volcanology of Holocene Airfall Deposits from Mt Mazama, Crater Lake, Oregon*. University of Lancaster.

Conflict of Interest: The authors declare that the research was conducted in the absence of any commercial or financial relationships that could be construed as a potential conflict of interest.

Publisher's Note: All claims expressed in this article are solely those of the authors and do not necessarily represent those of their affiliated organizations, or those of the publisher, the editors and the reviewers. Any product that may be evaluated in this article, or claim that may be made by its manufacturer, is not guaranteed or endorsed by the publisher.